Star clusters in the interacting galaxy system Arp 284

Bradley W. Peterson,[1]⋆ Curtis Struck,[1]x⋆ Beverly J. Smith[2] and Mark Hancock[2,3]

[1]*Department of Physics and Astronomy, Iowa State University, Ames, IA 50011, USA*
[2]*Department of Physics and Astronomy, East Tennessee State University, Johnson City, TN 37614, USA*
[3]*Institute of Geophysics and Planetary Physics, University of California, Riverside, Riverside, CA 92521, USA*

ABSTRACT

We present results from a study of protoglobular cluster candidates in the interacting galaxy system Arp 284 (NGC 7714/5) using data from the *Hubble Space Telescope* (*HST*). Previous studies of the Antennae and M51 have suggested that the majority of young massive star clusters dissolve within 20 Myr due to mass loss. We use the evolutionary synthesis code STARBURST99 to estimate ages and extinctions for approximately 175 clusters visible with *HST*. We also use lower resolution *Galaxy Evolution Explorer* and ground-based Hα data to estimate the ages of the giant H II regions in which these clusters are found, and compare the *Spitzer* colours of these H II regions to those of star-forming regions in other interacting systems. The ages are also used to aid in the interpretation of *Chandra* X-ray data.

Clusters in the tidal tails of NGC 7714 are generally found to have ages less than 20 Myr, though observational limits make the significance of this result uncertain. Older clusters, though not numerous, have nearly the same spatial distribution within the imaged portion of NGC 7714 as young clusters. The cluster population in the bridge connecting the two galaxies appears to be older, but the data in this part of the system are too limited to draw firm conclusions. The ages of the giant H II regions in NGC 7714 are generally older than those of their constituent clusters, possibly indicating that the young clusters we detect are surrounded by their dispersed predecessors.

Key words: galaxies: individual: NGC 7714, NGC 7715 – galaxies: interactions – galaxies: star clusters.

1 INTRODUCTION

The study of star formation in interacting galaxies has been revolutionized by the *Hubble Space Telescope* (*HST*). One of the early results to emerge from *HST* was the discovery of a class of bright, blue clusters $\lesssim 300$ Myr old in the peculiar elliptical galaxy NGC 1275 (Holtzman et al. 1992). These young massive clusters (YMCs) were also found in the prototypical merger remnant NGC 7252, with ages ranging from 34 to 500 Myr, consistent with the age of the merger (Whitmore et al. 1993). Many more examples soon followed, in which it was found that the properties of these YMCs implied that they might be young globular clusters, though with higher abundances (Conti & Vacca 1994; Hunter, O'Connell & Gallagher 1994).

In interacting galaxy systems, in which star-forming regions are abundant, the high resolution of *HST* has allowed the study of star cluster demographics. Among the results to emerge from such studies is the apparent dissolution of young star clusters, also known as infant mortality. Fall, Chandar & Whitmore (2005) used evolution-

ary synthesis models to estimate the ages of clusters in the Antennae and found that 90 per cent of clusters vanish over each age dex from 10^6 up to 10^9 yr, suggesting that cluster dissolution continues over very long time-scales. In contrast, Bastian et al. (2005a) found in M51 that 70 per cent of clusters dissolve in the first 20 Myr, indicating that disruption is concentrated on short time-scales. Recent spectroscopic observations of star clusters in the Antennae, combined with more careful modelling of the star formation history of the system, does not show the long-term cluster mortality previously claimed (Bastian et al. 2009), thus this issue is still controversial.

Additional evidence for a short dissolution time-scale has been found in comparisons of cluster and field populations. Tremonti et al. (2001) obtained UV spectra and evolutionary synthesis models of both clusters and diffuse regions of the dwarf starburst galaxy NGC 5253. Unlike the clusters, the diffuse region spectra lacked indications of O-type stars. It was suggested that stars form entirely within clusters, which dissolve on ∼10 Myr time-scales, preventing short-lived O stars from ever entering the field population.

Early-stage disruption has been ascribed largely to the loss of gas left over from star formation, which is swept out of the cluster by stellar winds and massive star supernovae (SNe). The resulting mass loss drops the escape velocity below the stellar velocities,

⋆E-mail: bwp@iastate.edu (BWP); curt@iastate.edu (CS)

causing the cluster to expand and decrease in surface brightness. The departing stars disperse into the field population in $\sim$ few 10^7 yr (Bastian & Goodwin 2006; Goodwin & Bastian 2006). On longer time-scales ($\sim 10^8$ yr and longer), interactions with giant molecular clouds (Gieles et al. 2006) and tidal effects are expected to become significant disruption mechanisms.

If YMCs are progenitors of globular clusters, some of them must survive their most massive stars, as well as external effects that may lead to dissolution (de Grijs & Parmentier 2007). Interacting galaxy systems have high numbers of YMCs, making them ideal targets for cluster population studies. To date, too few interacting systems have been observed to definitively determine how rapidly and by what mechanism massive clusters dissolve. Further, both the Antennae and M51 are advanced interactions with complex star formation histories. It is necessary to confirm infant mortality in early-stage interactions where the star formation history is simpler, with a particular emphasis on covering a wide range of tidal environments.

In this paper, we focus on the early-stage interacting system Arp 284, which at a distance of 38.6 ± 2.7 Mpc (1 arcsec = 190 pc) according to the NASA/IPAC Extragalactic Data base (NED) has nearly 175 detected star-forming regions in archival *HST* images. We use *HST* colours and the evolutionary synthesis code STAR-BURST99 (SB99) to obtain age and reddening estimates for star-forming regions. We also use lower resolution ultraviolet (UV) data from the *Galaxy Evolution Explorer* (*GALEX*; Martin et al. 2005) and ground-based Hα to obtain age estimates for larger H II regions, and mid-infrared (mid-IR) colours from the *Spitzer Space Telescope* Infrared Array Camera (IRAC; Werner et al. 2002; Fazio, Hora & Allen 2004) to compare the H II regions to IR emission clumps found in other interacting systems. These age results are used to aid in the interpretation of the X-ray data of Smith, Struck & Nowak (2005a), which was obtained using *Chandra* (Weisskopf et al. 2002).

2 TIDAL STAR-FORMING ENVIRONMENTS OF ARP 284

The peculiar morphology of the Arp 284 system results from an off-centre collision between two disc galaxies, with the primary (NGC 7714) having roughly three times the mass of the companion (NGC 7715). The time of closest approach was $\sim$100 Myr ago. For a discussion of the interaction history of the system, the reader is directed to the models of Struck & Smith (2003). In this section, we summarize previous observations of the Arp 284 system that relate to its star formation history. Most of the tidal features are labelled in Fig. 1, while the H II region complexes in the primary disc are labelled in Fig. 2.
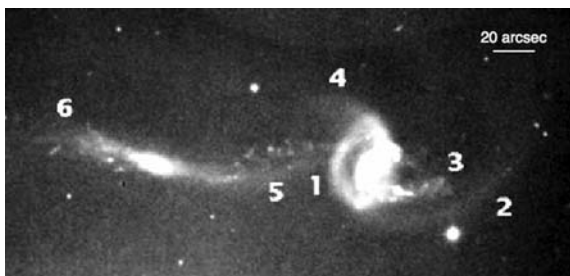

Figure 1. Optical photograph of Arp 284 from Arp (1966), with numbers labelling the prominent tidal features. North is up and east to the left. The field of view is 4.5×2.2 arcmin^2.
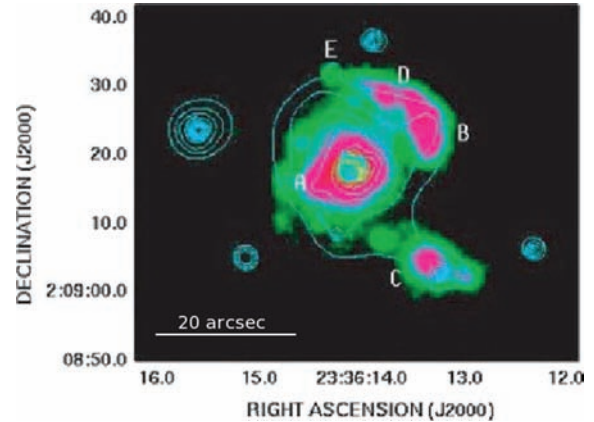

Figure 2. NGC 7714 disc indicating H II regions from Smith et al. (2005a). The colour scale shows Hα. The contours are a *Chandra* 0.3–8 keV X-ray map.

2.1 Nucleus of NGC 7714

The NGC 7714 nucleus was the first object to be described using the term 'starburst,' although there are earlier references in the literature to 'bursts of star formation' (Weedman et al. 1981). Strong Hα emission indicates a large nuclear H II region and ongoing star formation (González Delgado et al. 1995; Smith, Struck & Pogge 1997). O and B stars are required to fit the UV spectrum, with a best-fitting age $\sim$5 Myr and a burst of star formation favoured over continuous star formation (González Delgado et al. 1999).

Lançon et al. (2001) found that a second, older nuclear population is suggested by strong absorption bands of CO in the near-IR. In particular, the K-band spectrum is compatible with a combination of red supergiants, asymptotic giant branch stars and red giant branch stars. They concluded that a two-component model is probably an oversimplification of the nuclear star formation history, preferring a star formation rate that has decreased over several 10^8 years, either through a smooth exponential decrease or through a series of successively smaller bursts. The burst model best fits the observed SN rate with a burst 15–50 Myr ago, in addition to the most recent burst 5 Myr ago.

Infrared Space Observatory and *Spitzer* mid-IR spectra of the nuclear region show strong features from polycyclic aromatic hydrocarbons (PAHs) as well as bright forbidden lines (O'Halloran et al. 2000; Brandl et al. 2004). The metallicity of NGC 7714 peaks in the nucleus, with a value near $0.5Z_\odot$, and generally decreases with distance from the nucleus (González Delgado et al. 1995).

2.2 Stellar ring of NGC 7714 (feature 1)

NGC 7714 has a partial ring-like structure to the east. This feature does not show prominent Hα emission, reflecting a lack of ongoing star formation, while the red continuum suggests an old stellar population (González Delgado et al. 1995; Smith et al. 1997). Low levels of H I emission indicate that there is little hydrogen gas (Smith et al. 1997).

2.3 Southern tails of NGC 7714 (features 2 and 3)

Two parallel tidal tails lie to the south-west of the NGC 7714 nucleus. The outer southern tail, faintly visible in optical images, is revealed by 21-cm maps to be part of a large H I loop which reconnects with the galaxy in the northern tail (Smith & Wallin 1992;
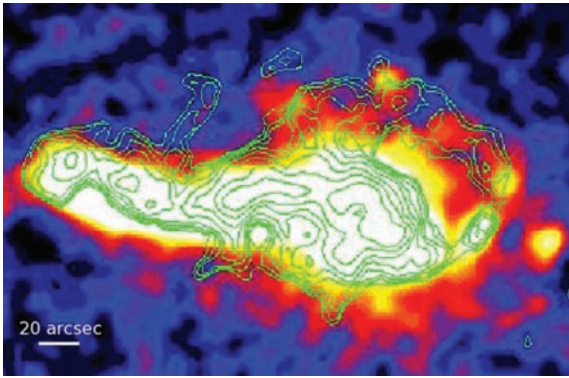
Figure 3. Smoothed *GALEX* FUV (colour) overlaid with Very Large Array H I (contours). Note that the western tail loops back to the main galaxy, and this ring-like feature is present in both H I and UV. The field of view is $5.1 \times 3.5 \, \text{arcmin}^2$.

Smith et al. 1997). The loop is also visible in *GALEX* far-UV (FUV), which is shown smoothed with overlaid H I contours in Fig. 3. This gas loop is an entirely separate structure from the inner southern tail, which hosts significant ongoing star formation.

The base of the inner southern tail just south of the nucleus contains H II region A (Smith et al. 2005a). This region is visible in 20-cm radio continuum (González Delgado et al. 1995; Smith et al. 1997). The *HST* images reveal numerous bright clusters along this structure, with another large H II region at the edge of the field (region C; González Delgado et al. 1995), coincident with a bright X-ray source (Smith et al. 2005a). The ages of regions A and C have been estimated by García-Vargas et al. (1997) at 5.0 ± 0.5 and 4.5 ± 0.5 Myr based on photoionization models. These regions also appear in *Spitzer* images (Smith et al. 2007), to be discussed below.

González Delgado et al. (1995) found Hα region A to have a metallicity comparable to the nucleus, about $0.5 \, \text{Z}_\odot$. Region C, at a larger distance from the nucleus, shows a lower metallicity of $0.25 \, \text{Z}_\odot$.

2.4 Northern tail of NGC 7714 (feature 4)

The northern tail of the primary galaxy is visible but not particularly prominent in optical photographs. Near the base of the tail, to the north-west of the nucleus, are Hα regions B, D and E. These regions are also detected in 21-cm H I emission and red continuum (Smith et al. 1997). *HST* resolves these regions into several smaller groups of clusters. The age of region D has been estimated at 3.5 ± 0.5 Myr using photoionization modelling (García-Vargas et al. 1997).

Hα region B has been found to have lower metallicity than the nucleus, about $0.25 \, \text{Z}_\odot$ (González Delgado et al. 1995).

2.5 Bridge (feature 5)

The bridge consists of a northern and a southern component. The northern bridge shows 'clumpy' emission from H I gas, and several Hα peaks are also found, offset slightly to the south, indicating ongoing star formation. The southern component lacks H I gas and Hα emission, but is readily seen in the red continuum, likely indicating an older stellar population (Smith et al. 1997). No metallicity data are currently available for the bridge.

2.6 Nucleus of NGC 7715

The lack of significant Hα emission in the NGC 7715 nucleus indicates that there is no ongoing massive star formation (González Delgado et al. 1995; Smith et al. 1997). Emission from the 21-cm H I radio line is also minimal, and offset to the north of the optical galaxy. The nucleus is comparatively bright in the red continuum, suggesting an aged stellar population (Smith et al. 1997). Spectral studies of the nucleus show a post-starburst spectrum, again confirming the lack of ongoing star formation (Bernlöhr 1993).

2.7 Eastern tail of NGC 7715 (feature 6)

The eastern tail of NGC 7715 is faintly seen in optical images. Radio maps show an H I counterpart, offset slightly to the north (Smith & Wallin 1992; Smith et al. 1997). Massive star formation is thought to be weak based on the lack of Hα emission. This feature has not been studied in detail, and it falls outside the field of the *HST* images. This poor coverage is unfortunate, because the models suggest that this tail curves behind the NGC 7715 disc, passes behind the bridge and comes back into view as the faint outer southern tail of NGC 7714 (Struck & Smith 2003). In this scenario, the tail contains a significant fraction of the original mass from the NGC 7715 disc (Struck & Smith 2003).

3 OBSERVATIONS

3.1 *HST* observations

The *HST* Wide Field and Planetary Camera 2 (WFPC2) has observed the Arp 284 system through several observing programmes between 1995 May 13 and 2001 July 10. These programmes targeted either the starburst nucleus or SN 1999dn in the disc of NGC 7714. The disparate nature of the observations means that many of the bright clusters are not visible in all filters, and in some cases the clusters were not found on the same chip across all filters. The field of view is $36 \times 36 \, \text{arcsec}^2$ on the PC chip and $80 \times 80 \, \text{arcsec}^2$ for the wide-field (WF) chips, with pixel sizes of $0.05 \, \text{arcsec pixel}^{-1}$ on the PC chip and $0.1 \, \text{arcsec pixel}^{-1}$ on the WF chips. The images and exposure times are summarized in Table 1. Note that the number in the filter name approximately corresponds to the central wavelength of the filter in nanometres. The available filters were F380W ($\sim U$), F555W ($\sim V$), F606W ($\sim R$) and F814W ($\sim I$).

The NGC 7714 nucleus and most of the inner southern tail are visible on the PC chip in all filters. One image in both F380W and F814W had to be discarded due to excessive cosmic ray contamination. This left three good images in the F380W filter, two in F555W, one in F606W and three in F814W. In F814W, H II region C was visible in two images on the WF4 chip.

The entire northern tail was visible on the PC chip in the F380W and F606W filters. In F555W and F814W, only 12 clusters were visible on the PC chip, with the remainder visible on WF4 in F814W.

The bridge was on the seam between the WF3 and WF4 chips in all four F380W images, so some of the clusters could not be measured in this band. In the other filters, it was always on the WF3 chip, with two images in F555W, one in F606W and two in F814W.

3.2 H II region observations

Archival *GALEX* and *Spitzer* IRAC data are available for the Arp 284 system. The *GALEX* images increase the number of colours that

Table 1. *HST* WFPC2 imaging of NGC 7714/5.

Data set	Exposure (s)	Filter	H II Regions in PC chip	H II Regions in WF chip	Comment
U3GQ0201R	500	F380W	Nucleus,A,B,part C,D,E	Bridge	Bridge split WF3/4
U3GQ0202R	500	F380W	Nucleus,A,B,part C,D,E	Bridge	Bridge split WF3/4
U3GQ0203R	400	F380W	Nucleus,A,B,part C,D,E	Bridge	CR on PC chip Bridge split WF3/4
U3GQ0204M	400	F380W	Nucleus,A,B,part C,D,E	Bridge	Bridge split WF3/4
U6A01601R	350	F555W	Nucleus,A,E	Bridge	
U6A01602R	350	F555W	Nucleus,A,E	Bridge	
U2E68801T	500	F606W	Nucleus,A,B,part C,D,E	Bridge	
U6A01701R	350	F814W	Nucleus,A	B,C,part D	
U6A01702R	350	F814W	Nucleus,A	B,C,part D	
U6A01801R	350	F814W	Nucleus,A, E	Bridge	
U6A01802R	350	F814W	Nucleus,A, E	Bridge	CR on PC chip
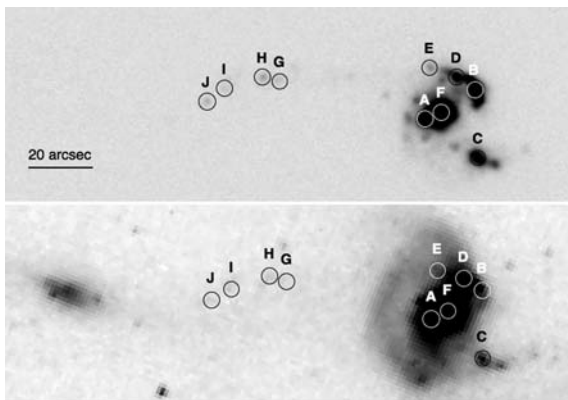
Figure 4. H II regions in Hα (top panel) and *Spitzer* 3.6 μm (bottom panel). The aperture radii have an angular size of 2.45 arcsec, and are also shown on the *HST* images in Figs 7–12. The field of view is 2.4×0.9 arcmin^2.

can be fit with SB99 models, while *Spitzer* colours can be compared to those of star-forming regions in other interacting systems. These instruments have significantly lower resolution than *HST*, but still allow the H II regions A–E to be resolved, as shown in Fig. 4. Each of these regions contains numerous star clusters resolved by *HST*. For clarity, the point-like sources in the *HST* data will be called 'clusters' while these larger structures will be called 'H II regions.' With Hα luminosities of $10^{39}–10^{41}$ erg s^{-1} (Smith et al. 2005a), these are properly classified as 'giant H II regions' (e.g. Kennicutt 1984).

The H II regions were located in an Hα map, which was then registered to the other images. The Hα and accompanying *R*-band images were obtained using the 1.8-m Perkins Telescope of the Ohio State University, using a CCD with a pixel size of 0.49 arcsec pixel^{-1}. These data were published previously in Smith et al. (1997).

GALEX observations are available in both the FUV and near-UV (NUV) bands, with effective wavelengths of 1516 and 2267 Å . The pixel size is 1.5 arcsec pixel^{-1}, which makes even these relatively large H II regions difficult to identify. The integration times are 4736 s in FUV and 520 s in NUV.

IR data from *Spitzer* are available for both the IRAC and Multi-band Imaging Photometer for *Spitzer* (MIPS) instruments. The resolution in the MIPS bands is far too low for cluster studies, and there are pronounced artefacts due to the point spread function because of the brightness of the nucleus, so only the broad-band IRAC

bands (3.6, 4.5, 5.8 and 8.0 μm) were used. The data reduction and mosaicking for the *Spitzer* data are described in Smith et al. (2007).

4 *HST* DATA ANALYSIS

4.1 Data reduction

All of the images were processed by the standard Hubble pipeline. The small number of exposures available in some data sets made cosmic ray removal a non-trivial task, since median combining two images is ineffective. First, we used the IRAF[1] task COSMICRAYS to remove events a few pixels in size that were well above background. Next, images were blinked to identify remaining cosmic rays, which were removed manually using the FIXPIX task. Finally, images were combined using the IMCOMBINE task. For F606W, only one image was available, so other filters were used for comparison.

4.2 Cluster selection

Clusters were selected using the IRAF task DAOFIND. The background level σ was determined using IMSTAT in a relatively dark part of the image. The nuclear region is much brighter than the rest of the disc, so it was necessary to use a higher background for cluster detection, measured at the outer edge of the nucleus. We used DAOFIND in each filter and then merged the lists to obtain the final sample. Clusters detected in only two filters were not included in the sample.

We detected 16 clusters in the nucleus at the 5σ level. The nucleus is quite crowded, so no attempt was made to push the detection threshold any lower. The lowest detected flux was 2.28×10^{-17} erg s^{-1} cm^{-2} Å^{-1} in F814W.

In the southern tail, 60 clusters were detected at the 5σ level and another 34 were detected at the 3σ level. These levels correspond to fluxes of 2.17 and 1.32×10^{-19} erg s^{-1} cm^{-2} Å^{-1}, respectively, in F814W. Before using the software, clusters in this part of the system were selected by eye. The 3σ set matched well with the results of the visual inspection, and were retained for the analysis.

In the northern tail, DAOFIND detected 60 clusters at the 5σ level, with no additional clusters detected at the 3σ level. This is probably due to crowding in the major complexes, which resulted in multiple detections on single clusters at lower detection thresholds. These clusters may in fact represent multiple unresolved star clusters. In a

---

[1] IRAF is distributed by the National Optical Astronomy Observatories, which are operated by the Association of Universities for Research in Astronomy, Inc., under cooperative agreement with the National Science Foundation.

few cases, multiple resolved clusters had to be measured in a single aperture because they were too close together to measure without aperture overlap.

Cluster selection was difficult in the bridge due to the higher background level in this part of the system and the lower resolution of the WF3 chip compared to the PC chip. For these reasons, it was necessary to lower the detection threshold in the bridge to 2σ, allowing the detection of 34 clusters. The faintest flux detected in F814W was 2.17×10^{-19} erg s^{-1} cm^{-2} Å^{-1}. Note that this is higher than the 3σ level on the PC chip. Only 23 of the clusters could be measured in F380W.

4.3 Photometry of clusters

Photometry was performed using the IRAF task PHOT in the DAOPHOT package, with magnitudes calibrated to the Vega magnitude system using the zero-point values given in the WFPC2 data handbook. The magnitudes and ages for the cluster sample are given in Table 2, while the extinctions and mass estimates are given in Table 3. The determination of the ages and extinctions will be discussed in Section 5.2. The mass determination will be discussed in Section 6.2.

The tidal tails generally fell on the PC chip. For these clusters, we used aperture radii of 3 or 4 pixels for single clusters, depending on crowding, and 6 pixels in six cases when barely resolved clusters had to be measured in a single aperture. Sky brightness for background subtraction was determined by the mode of the pixel values in an annulus of 10–15 pixels, centred on the cluster. In F814W, most of the northern tail was on the WF4 chip. These were measured using apertures with 2-pixel radii, or 3-pixel apertures for the poorly resolved groups, with sky subtraction determined by the mode in a 5–8 pixel annulus. These sizes were chosen because the WF chips have approximately twice the angular size of the PC chip, so the

Table 2. Cluster magnitudes and age estimates. The full table is available in the electronic version of the article (see the Supporting Information).

ID	F380W (mag)	F555W (mag)	F606W (mag)	F814W (mag)	Age (Z$_\odot$) (Myr)	Age (0.4 Z$_\odot$) (Myr)	Age (0.2 Z$_\odot$) (Myr)
1	22.46 ± 0.06	–	22.64 ± 0.03	22.18 ± 0.05	15^{+1}_{-6}	15^{+3}_{-1}	15^{+3}_{-1}
2	23.30 ± 0.14	–	22.84 ± 0.06	23.10 ± 0.15	4^{+2}_{-2}	5^{+2}_{-2}	5^{+4}_{-1}
3	22.33 ± 0.07	–	21.23 ± 0.03	21.67 ± 0.07	1^{+1}_{-1}	2^{+2}_{-2}	3^{+1}_{-2}
4	22.46 ± 0.08	–	22.02 ± 0.04	22.09 ± 0.08	6^{+1}_{-2}	6^{+1}_{-1}	7^{+8}_{-2}
5	21.25 ± 0.04	–	20.86 ± 0.02	21.06 ± 0.04	5^{+1}_{-1}	5^{+1}_{-1}	6^{+1}_{-1}
6	22.18 ± 0.06	–	22.04 ± 0.03	22.28 ± 0.09	5^{+1}_{-2}	5^{+1}_{-1}	6^{+1}_{-1}
7	21.00 ± 0.03	–	21.30 ± 0.02	21.07 ± 0.03	5^{+1}_{-1}	14^{+1}_{-1}	15^{+1}_{-1}
8	22.80 ± 0.11	–	21.78 ± 0.04	21.89 ± 0.05	3^{+1}_{-1}	4^{+1}_{-1}	4^{+2}_{-1}
9	20.84 ± 0.03	–	20.82 ± 0.04	20.74 ± 0.07	5^{+1}_{-1}	14^{+1}_{-3}	15^{+1}_{-2}
10	21.13 ± 0.04	–	21.43 ± 0.03	21.07 ± 0.05	15^{+1}_{-1}	14^{+1}_{-2}	15^{+1}_{-1}
11	22.89 ± 0.11	–	22.27 ± 0.05	21.94 ± 0.13	32^{+94}_{-27}	21^{+109}_{-15}	20^{+102}_{-12}
12	23.39 ± 0.17	–	22.97 ± 0.09	22.71 ± 0.16	35^{+74}_{-30}	20^{+79}_{-15}	20^{+75}_{-13}
13	21.41 ± 0.05	–	21.51 ± 0.03	21.17 ± 0.07	6^{+1}_{-1}	14^{+2}_{-1}	15^{+1}_{-2}
14	22.30 ± 0.10	–	21.62 ± 0.07	21.89 ± 0.22	3^{+3}_{-2}	4^{+3}_{-2}	5^{+4}_{-3}
15	21.89 ± 0.07	–	21.73 ± 0.04	21.04 ± 0.06	15^{+13}_{-4}	21^{+3}_{-5}	20^{+4}_{-4}

Table 3. Cluster $E(B - V)$ and mass estimates. The full table is available in the electronic version of the article (see the Supporting Information).

ID	$E(B - V)$ Z$_\odot$	$E(B - V)$ 0.4 Z$_\odot$	$E(B - V)$ 0.2 Z$_\odot$	M (10^6 M$_\odot$) Z$_\odot$	M (10^6 M$_\odot$) 0.4 Z$_\odot$	M (10^6 M$_\odot$) 0.2 Z$_\odot$
1	0^{+0}_{-0}	0^{+0}_{-0}	$0^{+0.04}_{-0}$	0.029	0.029	0.029
2	$0.16^{+0.12}_{-0.16}$	$0.12^{+0.12}_{-0.12}$	$0.12^{+0.12}_{-0.12}$	0.012	0.012	0.013
3	$0.24^{+0.06}_{-0.06}$	$0.22^{+0.10}_{-0.08}$	$0.24^{+0.06}_{-0.10}$	0.047	0.053	0.061
4	$0^{+0.18}_{-0}$	$0^{+0.06}_{-0}$	$0^{+0.18}_{-0}$	0.013	0.013	0.013
5	$0.06^{+0.06}_{-0.04}$	$0.10^{+0.04}_{-0.04}$	$0.06^{+0.04}_{-0.04}$	0.042	0.074	0.065
6	$0^{+0.08}_{-0}$	$0^{+0.04}_{-0}$	$0^{+0.04}_{-0}$	0.011	0.017	0.017
7	0^{+0}_{-0}	0^{+0}_{-0}	0^{+0}_{-0}	0.081	0.074	0.051
8	$0.4^{+0.08}_{-0.08}$	$0.38^{+0.08}_{-0.08}$	$0.34^{+0.08}_{-0.08}$	0.075	0.086	0.067
9	0^{+0}_{-0}	0^{+0}_{-0}	0^{+0}_{-0}	0.110	0.100	0.070
10	0^{+0}_{-0}	0^{+0}_{-0}	0^{+0}_{-0}	0.081	0.074	0.081
11	$0^{+0.24}_{-0}$	$0.08^{+0.18}_{-0.08}$	$0.08^{+0.22}_{-0.08}$	0.063	0.067	0.074
12	$0^{+0.22}_{-0}$	$0^{+0.22}_{-0}$	$0^{+0.26}_{-0}$	0.024	0.024	0.039
13	0^{+0}_{-0}	0^{+0}_{-0}	0^{+0}_{-0}	0.074	0.067	0.031
14	$0.18^{+0.22}_{-0.14}$	$0.18^{+0.16}_{-0.16}$	$0.22^{+0.12}_{-0.22}$	0.053	0.043	0.031
15	$0^{+0.06}_{-0}$	$0.06^{+0.08}_{-0.06}$	$0.08^{+0.08}_{-0.08}$	0.145	0.142	0.083

same area of sky was measured regardless of which chip a cluster fell on. Very little of the northern tail was visible in F555W.

The nucleus was always on the PC chip, but required the use of smaller apertures with radii of 2 or 3 pixels due to crowding. Background levels were determined by the mode in a 10–15 pixel annulus.

The bridge was generally on the WF3 chip. In F380W, the bridge unfortunately straddled the WF3 and WF4 chips, so a few clusters could not be observed in this filter. The aperture radius was 3 pixels, with background determined by the median in an 8–13 pixel annulus. This aperture size was selected because bridge clusters are often isolated, but there are several areas where multiple emission sources are packed closely together. In such cases, DAOFIND generally detected only one or two of the brightest sources, which were always sufficiently separated to be measured individually.

Aperture corrections could not be determined on the images. It was therefore necessary to use the standard corrections prescribed by Holtzman et al. (1995). The corrections for WF3 were used for all of the WF chips. Standard corrections are not given for the F380W or F606W filters, so corrections for the F336W and F555W, respectively, were used. The corrections were typically $\lesssim 0.3$ mag.

4.4 H II region photometry

In addition to the five regions A–E, we measured the nucleus (designated region F) and four regions (G–I) in the northern part of the bridge, shown in Hα and *Spitzer* 3.6 μm in Fig. 4. The *GALEX* and *Spitzer* images were registered to the *HST* data so that age estimates could be obtained using the total flux in the *HST* bands. This also allowed identification of the clusters making up the H II regions. Most of region C was off frame in all of the *HST* bands except F814W. Region G could not be measured at 4.5 μm because of a cosmic ray.

The aperture radius was selected as 2.45 arcsec (5 pixels on the Hα image) in all instruments to ensure that the same area of sky was represented at all wavelengths. The sky annulus widths were 1.82 arcsec in *HST*, 2.45 arcsec in Hα, 4.5 arcsec in *GALEX* and 3.6 arcsec in *Spitzer*. The measurements were not aperture corrected because the *HST* apertures were largely empty, and the emission regions were highly pixelated in *GALEX* and *Spitzer*.

Table 4 summarizes the photometric measurements. The Hα and *R* bands were calibrated to standard units using the results of James et al. (2004). The ratio of the Hα flux to *R* flux density provided an estimate of the equivalent width of the Hα line, EW(Hα). This equivalent width is included in the SB99 models and provides another method for determining the ages of the emission regions. Ages are presented in Table 5 and extinctions in Table 6. These will be discussed in Section 6.3.

5 *HST* RESULTS

5.1 Cluster colours

Colour–colour diagrams are shown in Fig. 5. In the top-left panel, we plot the magnitude in the F555W filter minus the magnitude in the F606W filter (F555W–F606W) versus (F606W–F814W) for all detected clusters for which these colours were available. The curves show SB99 instantaneous star formation models with $0.2\,Z_\odot$ metallicity for $E(B-V) = 0$ (solid curve), 0.24 (dashed curve) and 0.5 (dot–dashed curve) for ages from 10^6 to 10^{10} years. The youngest ages are at the lowest values of (F606W–F814W). The models are shown to give a sense of the effect of reddening, and it should be

Table 4. H II region photometry.

Region	FUV[a]	NUV[a]	F380W[a]	F555W[a]	F606W[a]	F814W[a]	Hα[b]	3.6 μm[c]	4.5 μm[c]	5.8 μm[c]	8.0 μm[c]
A	2080 ± 95	1890 ± 81	549 ± 4	396 ± 1	459 ± 1	276 ± 1	139 ± 14	2.56 ± 0.07	1.58 ± 0.04	8.48 ± 0.12	24.9 ± 0.3
B	1130 ± 110	474 ± 63	468 ± 4	–	202 ± 2	110 ± 2	92.9 ± 9.4	0.431 ± 0.010	0.391 ± 0.006	1.01 ± 0.05	2.69 ± 0.23
C	1550 ± 80	551 ± 40	–	–	–	153 ± 1	52.8 ± 5.3	0.235 ± 0.019	0.235 ± 0.010	0.553 ± 0.034	1.20 ± 0.10
D	500 ± 91	236 ± 58	258 ± 3	–	140 ± 1	86.2 ± 1.7	32.0 ± 3.5	0.357 ± 0.061	0.255 ± 0.048	0.980 ± 0.119	2.42 ± 0.34
E	≤218 ± 25	≤64.8 ± 21.2	15.8 ± 3.0	–	11.2 ± 0.7	–	7.32 ± 0.79	≤0.141 ± 0.011	≤0.0851 ± 0.0150	≤0.365 ± 0.050	≤1.37 ± 0.09
F	13600 ± 100	6220 ± 110	13200 ± 100	9080 ± 10	8610 ± 10	5690 ± 10	1140 ± 110	14.5 ± 0.1	12.9 ± 0.1	40.2 ± 0.2	114 ± 1
G	≤70.3 ± 11.2	≤22.4 ± 8.3	–	17.2 ± 0.4	16.9 ± 0.4	8.32 ± 0.28	2.8 ± 0.3	0.0152 ± 0.0034	–	0.0552 ± 0.0127	0.105 ± 0.015
H	≤93.2 ± 10.4	≤43.2 ± 6.5	–	27.6 ± 0.4	25.2 ± 0.4	10.9 ± 0.3	4.87 ± 0.51	0.0305 ± 0.0035	0.0193 ± 0.003	0.0804 ± 0.0101	0.154 ± 0.011
I	≤39.2 ± 7.3	≤32.0 ± 5.9	–	14.9 ± 0.4	14.8 ± 0.4	9.73 ± 0.27	2.02 ± 0.23	0.0259 ± 0.0032	0.0186 ± 0.003	0.0665 ± 0.0107	0.221 ± 0.015
J	≤41.0 ± 6.3	≤34.8 ± 5.7	–	10.4 ± 0.4	13.0 ± 0.4	5.07 ± 0.28	3.50 ± 0.36	0.0211 ± 0.0033	0.0111 ± 0.005	0.0609 ± 0.0108	0.159 ± 0.012

[a] FUV, NUV, F380W, F555W, F606W, F814W in units of 10^{-18} erg s^{-1} cm^{-2} Å^{-1}.
[b] Hα in units of 10^{-15} erg s^{-1} cm^{-2}.
[c] 3.6, 4.5, 5.8, 8.0 μm in units of mJy.

Table 5. H II region ages (Myr).

Region	Age (inst)[a] 0.4 Z_⊙	Age (inst)[a] 0.2 Z_⊙	Age (cont)[a] 0.4 Z_⊙	Age (cont)[a] 0.2 Z_⊙	Med. Age[b] 0.4 Z_⊙	Med. Age[b] 0.2 Z_⊙	EW(Hα) Å	EW(Hα) Age 0.4 Z_⊙	EW(Hα) Age 0.2 Z_⊙	Lit. Age[c]	f_c^d	$L_{H\alpha}/L_X^e$
A	10^{+1}_{-1}	10^{+1}_{-1}	1^{+1}_{-1}	1^{+1}_{-1}	5^{+1}_{-1}	5^{+2}_{-2}	29.8 ± 3.3	10^{+0}_{-1}	11^{+0}_{-0}	5 ± 0.5	0.18	22
B	273^{+65}_{-96}	88^{+16}_{-18}	489^{+273}_{-207}	128^{+1272}_{-42}	14^{+1}_{-1}	15^{+1}_{-2}	39.6 ± 5	9^{+0}_{-0}	10^{+0}_{-0}	3.5 ± 0.5	0.26	11
C	–	–	–	–	–	–	27.3 ± 3	10^{+0}_{-1}	11^{+0}_{-1}	4.5 ± 0.5	–	6.1
D	292^{+135}_{-234}	87^{+84}_{-82}	497^{+1103}_{-435}	1200^{+900}_{-1195}	16^{+4}_{-8}	17^{+3}_{-4}	22.4 ± 3.4	11^{+1}_{-0}	12^{+1}_{-1}	–	0.17	≥23
E	–	–	–	–	–	–	56.2 ± 21	8^{+2}_{-1}	9^{+1}_{-1}	–	–	3.1
F	222^{+6}_{-6}	86^{+1}_{-1}	421^{+12}_{-11}	2600^{+100}_{-100}	10^{+16}_{-2}	15^{+1}_{-1}	15 ± 1.6	12^{+0}_{-0}	14^{+1}_{-1}	5; 15 – 50	0.25	1.5
G	6^{+2}_{-1}	6^{+2}_{-1}	1^{+15}_{-1}	1^{+19}_{-1}	21^{+959}_{-15}	266^{+198}_{-257}	28.5 ± 7	10^{+1}_{-1}	11^{+1}_{-1}	–	0.06	–
H	6^{+1}_{-1}	6^{+1}_{-1}	1^{+8}_{-1}	2^{+8}_{-2}	182^{+36}_{-177}	68^{+24}_{-62}	27.3 ± 4.4	10^{+0}_{-1}	11^{+1}_{-0}	–	0.27	–
I	7^{+376}_{-2}	8^{+1092}_{-2}	1^{+3799}_{-1}	2^{+4298}_{-2}	13^{+12}_{-7}	120^{+74}_{-114}	12.1 ± 2.1	13^{+1}_{-1}	16^{+0}_{-1}	–	0.15	–
J	4^{+1}_{-1}	4^{+1}_{-1}	1^{+7}_{-1}	1^{+8}_{-1}	4^{+1}_{-1}	5^{+1}_{-1}	113 ± 82	6^{+3}_{-0}	7^{+3}_{-1}	–	0.31	–

[a] Ages in Myr from large-aperture broad-band photometry for instantaneous starburst (inst) and continuous star formation (cont) models.
[b] Median age of *HST*-resolved clusters in the region. These are useful only for regions A, B, D, F; see the text for explanation.
[c] Ages determined by photoionization modelling for A, B, C (García-Vargas et al. 1997). Ages for F determined by spectral line synthesis (Gonzáles Delgado et al. 1999) and SN rate (Lançon et al. 2001).
[d] Fraction of H II region luminosity contained in sample clusters in F814W.
[e] From Smith et al. (2005a).

noted that $0.2\,Z_\odot$ is not the observed metallicity for the nucleus and parts of the southern tail. The bridge population is generally bluer in (F555W–F606W) and redder in (F606W–F814W) than the populations of the other regions. The southern tail has the opposite tendency, leaning red in (F555W–F606W) and blue in (F606W–F814W). Only a few clusters in the northern tail were on frame in F555W; those that were tend towards more intermediate values in both colours. The nuclear population is similar.

The top-right panel shows all detected clusters in (F380W–F606W) versus (F606W–F814W), along with SB99 models. The youngest ages on the curves appear at the lowest values of (F606W–F814W). The middle and bottom panels show the same colours, with the different regions plotted separately and error bars shown. The differences between the populations are less striking in this colour combination than the one discussed above, and arise primarily in (F606W–F814W).

The median statistical uncertainties in the northern tail are 0.081 and 0.095 mag for (F380W–F606W) and (F606W–F814W), respectively. In the southern tail, the median uncertainties are 0.153 and 0.107 mag; in the nucleus 0.050 and 0.040 mag and in the bridge 0.167 and 0.123 mag. The uncertainties are large in the southern tail in part because it includes clumps detected at the 3σ level. If only 5σ level clumps are included, the median uncertainties are 0.114 in (F380W–F606W) and 0.088 in (F606W–F814W).

5.2 Age determination

Age and reddening estimates were obtained using the STARBURST99 v5.1 evolutionary synthesis code (Leitherer et al. 1999; Vázquez & Leitherer 2005). We modelled the colours of the clusters assuming a single, instantaneous burst of star formation with a Kroupa (2002) initial mass function over the range 0.1–$100\,M_\odot$. Spectral energy distributions (SEDs) were calculated for cluster ages of 1 Myr to 10 Gyr and included contributions from Hα emission. The SEDs were reddened from 0 to 2 mag of $E(B-V)$ using the reddening law of Calzetti, Kinney & Storchi-Bergmann (1994). These model spectra were convolved with the bandpasses of the four *HST* filters. The model age and extinction providing the best fit to the observations was determined using χ^2 minimization Uncertainties in both the ages and extinctions were determined as in Smith et al. (2008), and are driven largely by the degeneracy between age and reddening. Breaking this degeneracy is particularly difficult for clusters with coverage in only three filters. Such clusters generally have larger age uncertainties than those with that were covered in all four filters.

Models were run for three different metallicities: $Z_\odot$, $0.4\,Z_\odot$ and $0.2\,Z_\odot$. The $0.4\,Z_\odot$ model is representative of the spectroscopically measured abundances in the nucleus and H II region A, while the $0.2\,Z_\odot$ model is close to that of H II regions B and C. The solar composition models were used primarily for comparison.

Several colour combinations were used because not all clusters were available in all colours. Age estimates obtained from SB99 have been found to be most reliable when (1) a large number of colours and (2) the bluest available combination of colours are used. *U* coverage is particularly important (e.g. Hancock et al. 2008). We adhered to these results in determining which of the available colour combinations would provide the best age estimate for each cluster at each metallicity.

Our best-fitting ages for the clusters are given in Table 2, while $E(B-V)$ and masses are shown in Table 3. The age distributions within the features of the system are shown in Fig. 6. Finding charts showing the locations of the clusters are given in Figs 7–12, with

Table 6. H II region extinctions.

Region	$E(B-V)$ (inst) 0.4 Z$_\odot$	$E(B-V)$ (inst) 0.2 Z$_\odot$	$E(B-V)$ (cont) 0.4 Z$_\odot$	$E(B-V)$ (cont) 0.2 Z$_\odot$	Lit. $E(B-V)^a$
A	$0.22^{+0.02}_{-0.02}$	$0.14^{+0.02}_{-0.02}$	$0.36^{+0.02}_{-0.02}$	$0.34^{+0.02}_{-0.02}$	0.25
B	$0^{+0.06}_{-0}$	$0.12^{+0.08}_{-0.08}$	$0.12^{+0.08}_{-0.10}$	$0.18^{+0.08}_{-0.18}$	0.28
C	–	–	–	–	0.34
D	$0.10^{+0.14}_{-0.10}$	$0.20^{+0.08}_{-0.20}$	$0.18^{+0.12}_{-0.18}$	$0^{+0.48}_{-0}$	–
E	–	–	–	–	–
F	$0.18^{+0.02}_{-0.18}$	$0.28^{+0.02}_{-0.02}$	$0.26^{+0.02}_{-0.02}$	0^{+0}_{-0}	0.22; 0.08
G	$0.24^{+0.08}_{-0.24}$	$0.42^{+0.08}_{-0.20}$	$0.22^{+0.14}_{-0.08}$	$0.20^{+0.16}_{-0.08}$	–
H	$0.12^{+0.06}_{-0.06}$	$0.28^{+0.06}_{-0.18}$	$0.08^{+0.14}_{-0.06}$	$0.08^{+0.12}_{-0.06}$	–
I	$0.24^{+0.30}_{-0.16}$	$0.44^{+0.14}_{-0.44}$	$0.44^{+0.16}_{-0.44}$	$0.44^{+0.44}_{-0.44}$	–
J	$0.42^{+0.12}_{-0.12}$	$0.38^{+0.12}_{-0.12}$	$0.14^{+0.16}_{-0.12}$	$0.12^{+0.16}_{-0.12}$	–

^{a}A,B, C from González Delgado et al. (1995); F from González Delgado et al. (1995) (Balmer decrement) and González Delgado et al. (1999) (UV continuum).
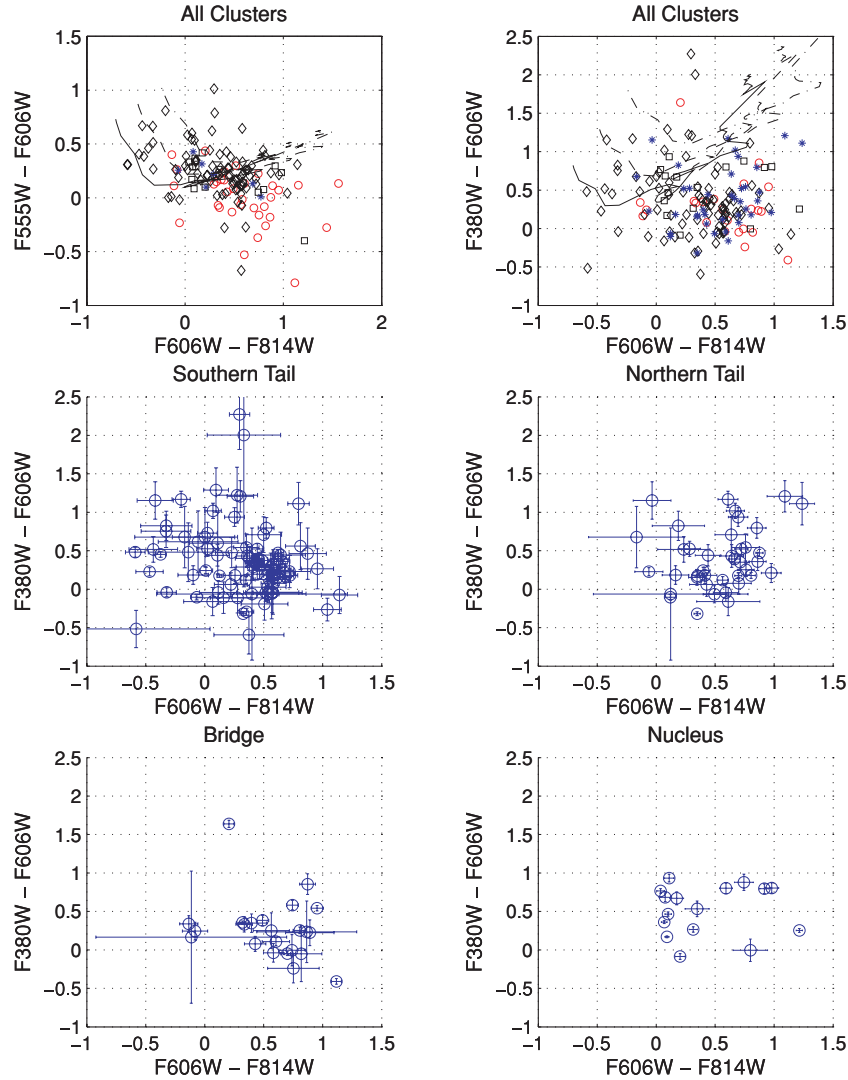
Figure 5. In the top panels, red circles represent clusters from the bridge, black diamonds the southern tail, blue asterisks the northern tail and black squares the nucleus. The curves show SB99 instantaneous star formation models with $0.2\,Z_\odot$ metallicity for $E(B-V) = 0$ (solid curve), 0.24 (dashed curve) and 0.5 (dot–dashed curve). These curves give a sense of the effect of reddening, but the metallicity is not representative of the nucleus or parts of the southern tail. The middle and bottom four panels show the same colours as the upper-right panel separated by region, with error bars.
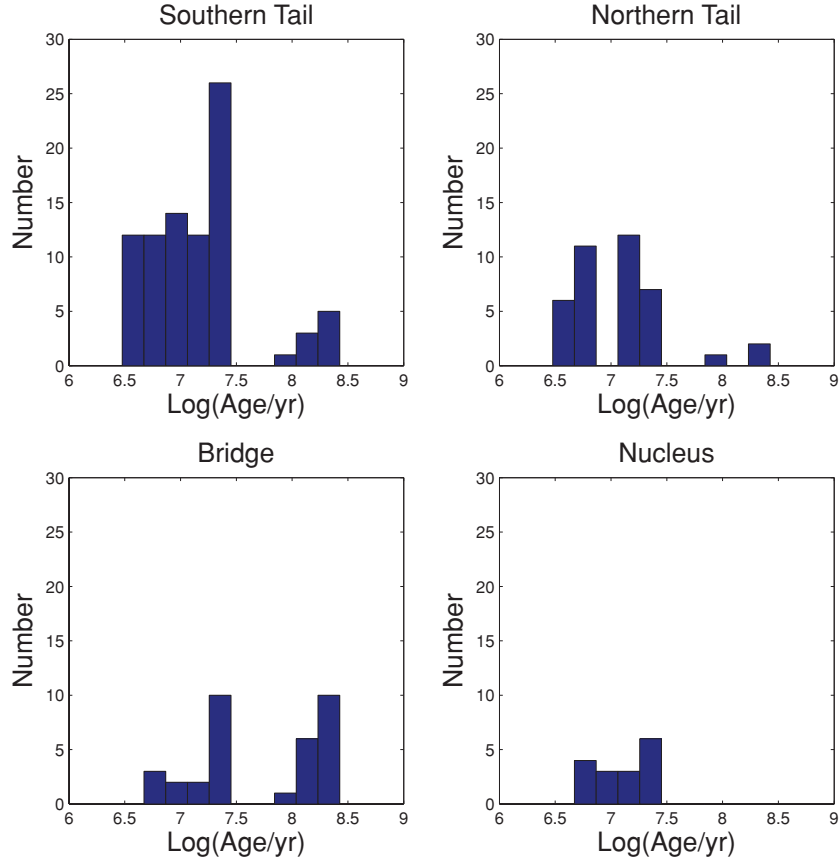
Figure 6. Histograms of cluster ages from $0.2\,Z_\odot$ models in the southern tail (top-left panel), northern tail (top-right panel) and bridge (bottom-left panel), and from the $0.4\,Z_\odot$ model in the nucleus (bottom-right panel).
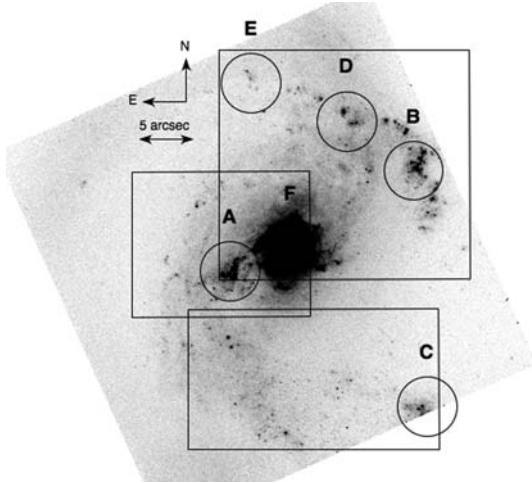

Figure 7. F606W image of NGC 7714 with northern, central and southern areas indicated. These areas are examined more closely in Figs 8–12. Several H II regions identified in lower resolution data are also indicated. Note that region C is partially off frame towards the bottom right of the box indicating the southern area.

circles indicating ages ≤10 Myr, diamonds 11–22 Myr and squares >22 Myr. The apertures used for photometry of the large H II regions are also shown. The clusters are generally very young, occupying the two younger age bins (1–10 and 11–22 Myr). Very few clusters older than 22 Myr are found in the tidal tails.
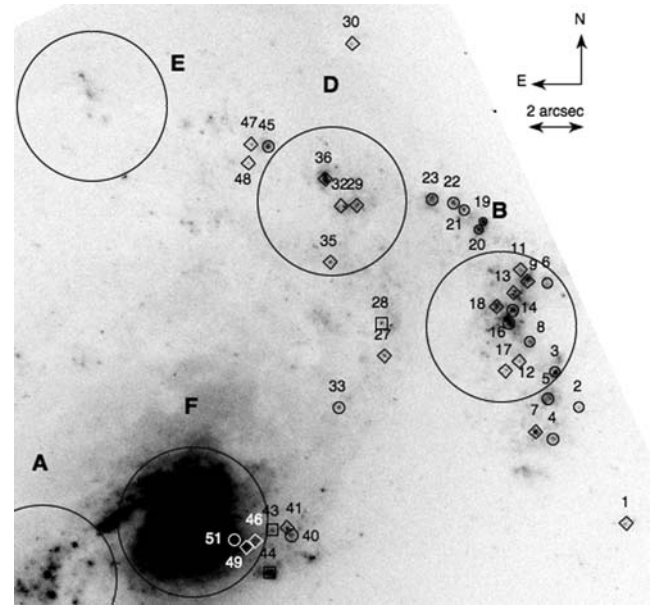
Figure 8. F606W image of the northern tail of NGC 7714, with ages indicated for all detected clusters for the $0.2\,Z_\odot$ models. Circles represent ages 1–10 Myr, diamonds 11–22 Myr, squares ≥23 Myr. The metallicities of H II regions B and D have been measured at $0.25\,Z_\odot$, while the nucleus has metallicity $0.5\,Z_\odot$. All clusters shown are considered part of the northern tail.
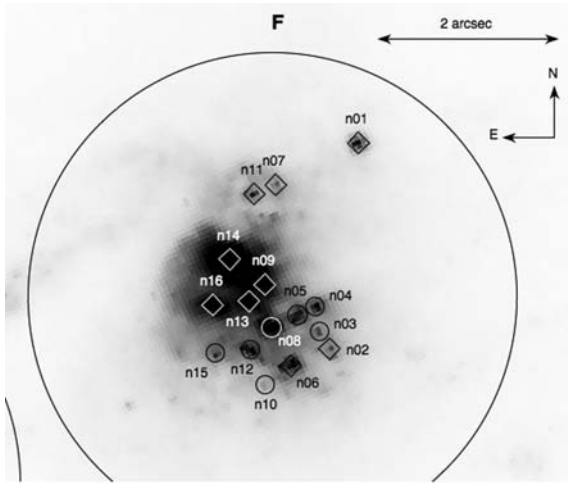
Figure 9. F606W image of the NGC 7714 nucleus with ages from the $0.4\,Z_{\odot}$ model indicated for all detected clusters. Circles represent ages 1–10 Myr, diamonds 11–22 Myr, squares $\geq$23 Myr. The metallicity has been measured at $0.5\,Z_{\odot}$.
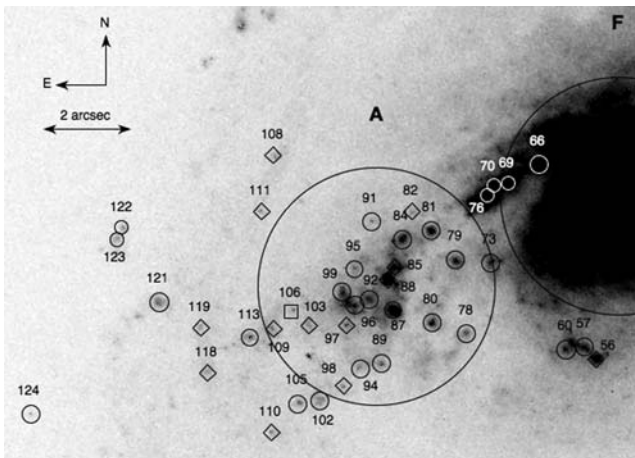
Figure 10. F606W image of the central region of NGC 7714 with ages from the $0.4\,Z_{\odot}$ model indicated for all detected clusters. Circles represent ages 1–10 Myr, diamonds 11–22 Myr, squares $\geq$23 Myr. The nucleus has a measured metallicity of $0.5\,Z_{\odot}$, so this model should give the best age estimates. These clusters are considered to be part of the southern tail.

Ages determined by evolutionary synthesis techniques generally have large uncertainties. In our sample, the uncertainties are typically very close to the ages. The median age is 14 Myr, with a median negative uncertainty of 5 Myr and a positive uncertainty of 10 Myr.

5.3 Luminosity function

The luminosities in the F814W band for the clusters $\Delta \nu L(\nu)$ were calculated using a distance of 39 Mpc (NED), using a bandwidth of 7.2×10^{13} Hz. The luminosity distribution, excluding the extremely luminous nuclear population, is shown in Fig. 13, and provides one estimate of our sample completeness. We assume a simple power law form for the luminosity function, defined by $n(L)\,\mathrm{d}L \propto L^{-\alpha}\,\mathrm{d}L$. A best-fitting line is determined after the distribution turns over, giving a slope of -1.3 with a completeness limit of $10^{5.1}\mathrm{L}_{\odot}$.

The uncertainty in the slope may be estimated as follows. The distribution has a flat top, so there are two reasonable possibil-

ities for the turnover point. Selecting as the completeness limit $10^{4.9}L_{\odot}$, we obtain a slope of -1.1. Our best estimate for the slope is -1.3 ± 0.2. Cluster luminosity functions typically have $\alpha = -2$ (e.g. Whitmore et al. 1999), which gives a slope of -1 when binned logarithmically. Our luminosity function is consistent with this trend to within the uncertainties.

6 DISCUSSION

6.1 *HST* cluster ages

The metallicities determined by González Delgado et al. (1995) aid in the interpretation of our evolutionary synthesis results. In the southern tail, H II region A has a measured metallicity $\sim 0.5\,Z_{\odot}$. The best age estimates should therefore come from our $0.4\,Z_{\odot}$ models, which show this region to be dominated by clusters with ages 10 Myr or less.

The metallicity of H II region C at the base of the southern tail is $\sim 0.25\,Z_{\odot}$ (González Delgado et al. 1995). Combined with the general metallicity gradient observed in the galaxy, we are led to favour the $0.2\,Z_{\odot}$ model in the western part of the southern tail, which shows more clusters older than 22 Myr than does the $0.4\,Z_{\odot}$ model. Note, however, that part of region C was off frame (Fig. 11), so we only have age estimates for two of its constituent clusters.

In the northern tail, the dependence of derived age on metallicity is less pronounced. Only five clusters change age bins between the 0.2 and $0.4\,Z_{\odot}$ models, all of which are near the nucleus. Most of the clusters are in H II regions B and D. These regions have measured abundances $\sim 0.25\,Z_{\odot}$, so our $0.2\,Z_{\odot}$ models should provide the best age estimates. The cluster ages are all less than 23 Myr in these models, with about half 10 Myr or younger. This is not unexpected, since this part of the northern tail is detected in Hα (Smith et al. 1997) and *Spitzer* 8 μm (Smith et al. 2007).

The metallicity of the nucleus has been measured at $\sim 0.5\,Z_{\odot}$, so the $0.4\,Z_{\odot}$ model is preferred here. Seven of the 16 clusters have ages $\leq$10 Myr, with the remainder between 14 and 21 Myr. The gap between these age populations is probably not significant, since the rapid evolution of red giants after 10 Myr makes exact age determination exceptionally difficult and often results in gaps between 10 and 15 Myr (e.g. Fall et al. 2005). The younger population fits well with the UV spectral results of González Delgado et al. (1999), while the older population fits with one of the bursts expected by Lançon et al. (2001).

Of the 124 clusters detected in the tidal tails of NGC 7714, those with ages $>$22 Myr number only five in the $0.4\,Z_{\odot}$ model and 12 in the $0.2\,Z_{\odot}$ model. If an age is assigned to each cluster based on the measured or most likely metallicity, there are eight older than 22 Myr. The small sample of 16 clusters detected in the nucleus has no clusters older than 22 Myr. There is little evidence in NGC 7714 of a population older than $\sim$20 Myr, despite an interaction that had closest approach $\sim$100 Myr ago. We also find that the cluster age groups are evenly distributed over the galaxy. The lack of older clusters detected in the nucleus may be due to the difficulty in detecting such clusters amidst the high background caused by YMCs.

These results are similar to those obtained by Bastian et al. (2005b) for the interacting galaxy NGC 6872. Most of the clusters in NGC 6872 were found by colour fitting to be younger than 30 Myr. These were spread throughout the galaxy, extending far out into the tidal tails. Clusters older than 30 Myr were concentrated in the central regions of the galaxy. However, the 'central regions' of NGC 6872 have a spatial size $\sim$30 kpc, while the imaged portion of
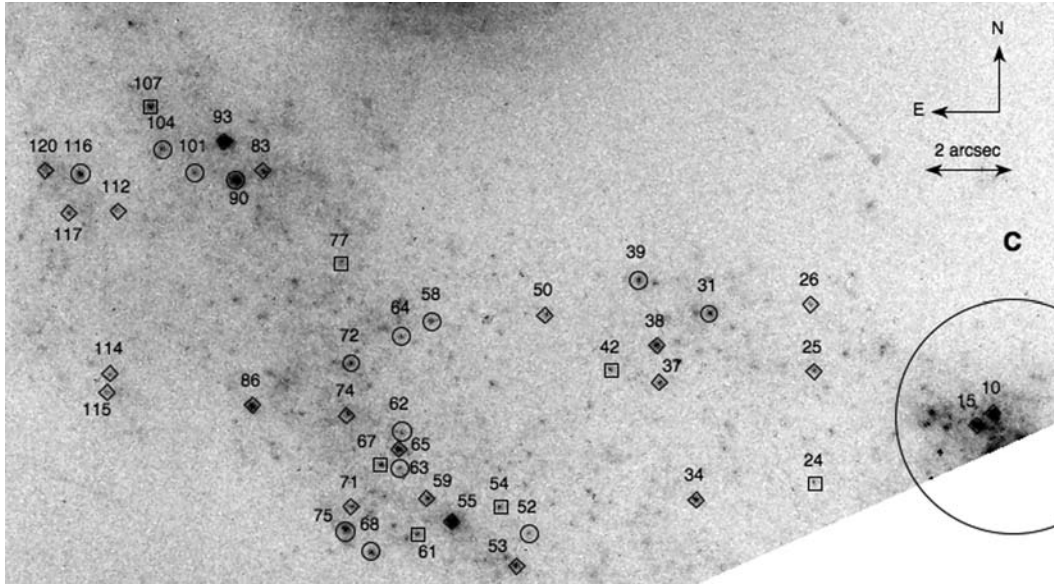
Figure 11. F606W image of the southern tail of NGC 7714 with ages from the $0.2\,Z_\odot$ models indicated for all detected clusters. Circles represent ages 1–10 Myr, diamonds 11–22 Myr, squares $\geq$23 Myr. Clusters 10 and 15 are inside H II region C, which has a measured metallicity of $0.25\,Z_\odot$
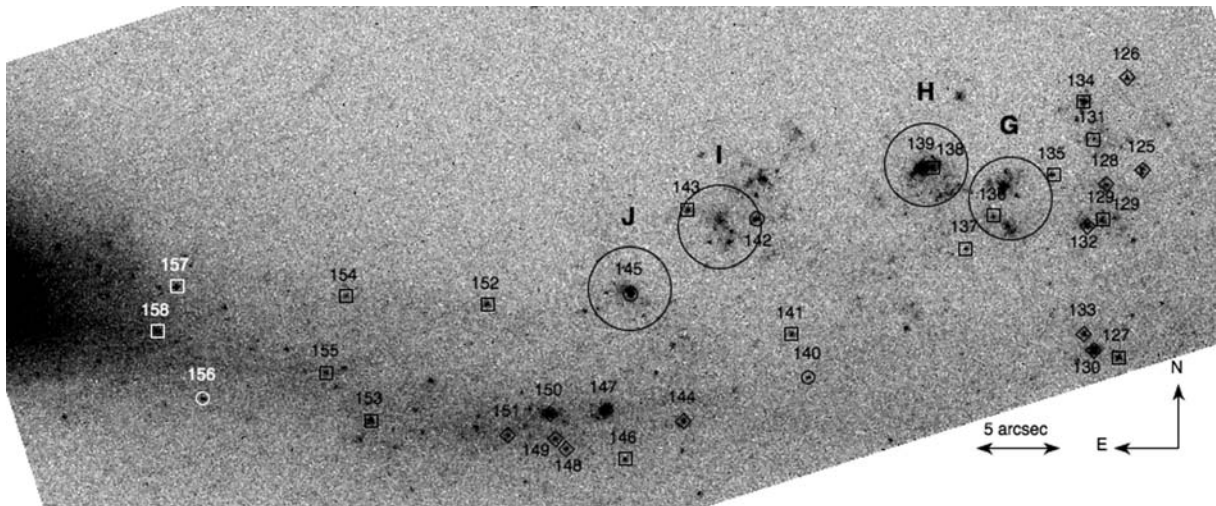

Figure 12. F555W image with all detected clumps in the bridge with ages from the $0.2\,Z_\odot$ models. Circles represent ages 1–10 Myr, diamonds 11–22 Myr, squares $\geq$23 Myr. The metallicity of the bridge has not been measured, but is likely to be low.

the NGC 7714 disc in our data is only $\sim$7 kpc. The age distribution within NGC 7714 is compatible with that found by Bastian et al. in NGC 6872, but a wider field will be required to determine if the concentration of old clusters is similar in the two galaxies.

The bridge ages are difficult to interpret because of the large colour uncertainties, incomplete coverage in F380W and lack of metallicity data. The metallicity in NGC 7714 generally decreases with distance from the nucleus. However, some of the bridge material may originate in NGC 7715, which has unknown metallicity. Nevertheless, a low metallicity is expected due to the abundances measured elsewhere in the system and because tidal features in interacting galaxies generally show low abundances.

Despite the large uncertainties, we note that the only evidence for a significant population with age $\gtrsim$100 Myr is in the bridge. Out of 34 clusters, the numbers with ages >22 Myr are 12 and 17 in the 0.4 and $0.2\,Z_\odot$ models, respectively. However, only one of these clusters has F380W data available in the $0.4\,Z_\odot$ case,

and nine in the $0.2\,Z_\odot$ case. The existence of an older population in the bridge is by no means certain, but if present could indicate that cluster dissolution mechanisms have acted more weakly here than in the tidal tails, which in this system are closer to the nucleus. Older clusters should survive more easily in the bridge because tidal forces are generally smaller there than in the tails. However, the gas expulsion mechanisms thought to be responsible for infant mortality operate independently from the tidal forces, so the rate at which very young clusters dissolve is not expected to change.

To address the issue of sample completeness, we begin with the luminosity function (Fig. 13). Cutting out clusters with luminosities below the completeness limit, we have 49 left in the tidal tails and only four in the bridge. The bridge sample is far too incomplete to permit any reliable analysis. Only two clusters in the tidal tails that survive the luminosity cut have ages >22 Myr, and those only in the $0.2\,Z_\odot$ model. It is unsurprising that older clusters would be
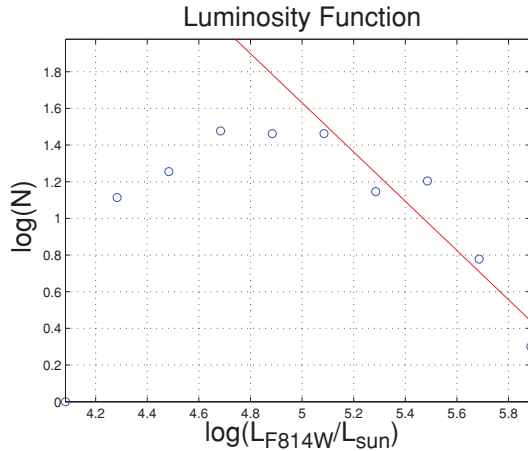
Figure 13. Luminosity distribution in F814W for all detected clusters outside the nucleus. The luminosity is defined as the luminosity in the F814W band $\Delta\nu L(\nu)$, where $\Delta\nu$ is the bandwidth of 7.2×10^{13} Hz. The solid red line is a power-law fit to the distribution after the turnover with slope of -1.3 ± 0.3, giving a completeness limit of approximately $(5.1 \pm 0.2) \times 10^5 \, L_\odot$.

preferentially cut from a luminosity-limited sample, since clusters get both redder and fainter as their stellar populations age.

6.2 *HST* cluster mass function

It is common practice in studies of cluster ages to use a mass cut-off rather than a luminosity cut-off. Due to evolutionary fading, clusters of a given age will remain above the luminosity limit only if they have a sufficiently high mass. Therefore, imposing a luminosity limit will generally undersample old clusters.

Mass estimates are based on the assumption that clusters of a given age all have the same mass-to-light ratio, with luminosity values calculated for clusters with mass $10^6 \, M_\odot$. The luminosity of a cluster relative to a $10^6 \, M_\odot$ cluster of the same age then gives an estimate of the mass. The uncertainties in the masses are quite large, up to a factor of ~ 2. Mass estimates based on the best-fitting age and extinction are shown in Table 3.

The lowest mass for which the sample is complete was determined assuming a simple power-law form for the cluster mass distribution. For $0.4 \, Z_\odot$, we obtain a reasonably good fit with a slope of ≈ -1.4 and a limiting mass of $10^{5.0} \, M_\odot$. The quality of the fit is not high due to a lack of clusters in the mass bin centred at $10^{6.0} \, M_\odot$, which may reflect the high uncertainties in masses determined in this way. The mass estimates for the $0.2 \, Z_\odot$ model produced a slope of -1.5, but with a lower mass limit at about $10^{4.8} \, M_\odot$. The mass distribution for the $0.2 \, Z_\odot$ model is shown in Fig. 14.

The uncertainties for the mass function fits may be estimated using the same technique as was used for the luminosity function. For the $0.4 \, Z_\odot$ model, the next best choice of limiting mass would be $10^{4.7} \, M_\odot$, which gives a slope of -1.0. In the $0.2 \, Z_\odot$ model, both $10^{4.5}$ and $10^{5.0} \, M_\odot$ are reasonable choices, producing slopes of -1.8 and -1.1, respectively. Using these alternate choices to estimate the uncertainties, the $0.4 \, Z_\odot$ model has a slope of -1.4 ± 0.4, with smaller values being more likely. For the $0.2 \, Z_\odot$ model, the slope is -1.5 ± 0.4. At the limits of the uncertainties, our mass functions agree with the typical power-law index near $\alpha = -2$, found for example in the Antennae (Zhang & Fall 1999) and Magellanic Clouds (Hunter et al. 2003). Due to the small size of
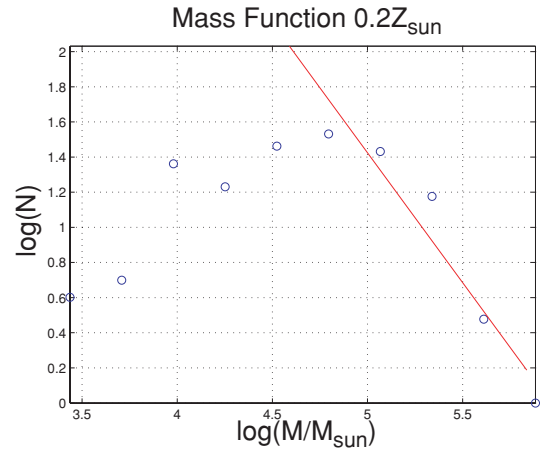

Figure 14. Cluster mass distributions for the $0.2 \, Z_\odot$ model. The solid red line is a power-law fit to the part of the distribution after the turn-over. The fit has slope of -1.5 ± 0.4 with a limiting mass $\sim 10^{4.8} \, M_\odot$.
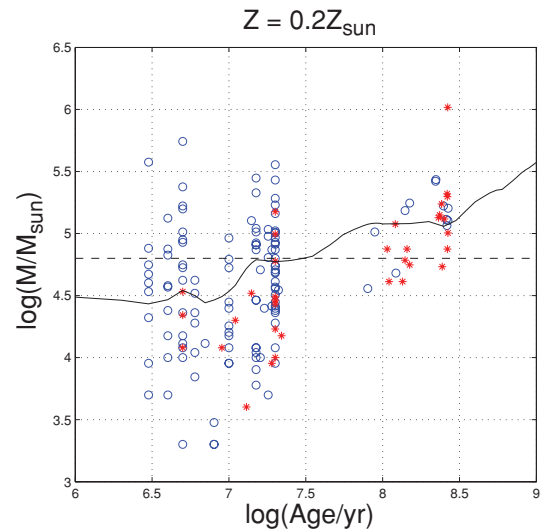

Figure 15. Mass versus age for the $0.2 \, Z_\odot$ model. Blue circles represent the NGC 7714 disc, while red asterisks are bridge clusters. The dashed black line represents the age-averaged mass completeness limit of $10^{4.8} \, M_\odot$ from Fig. 14. The solid black curve shows the mass of a cluster with an F840W luminosity equal to our completeness limit of $10^{5.1} \, L_\odot$, as a function of age.

our sample, we are unable to test the claim of Gieles (2009) that the cluster initial mass function is truncated at the high-mass end.

The completeness limit in mass, unlike that in luminosity, is a function of age due to evolutionary fading. Thus, the turn-over in Fig. 14 gives an age-averaged completeness limit for mass. For younger systems, the mass completeness limit is lower than for older systems. The masses are plotted against the ages for the $0.2 \, Z_\odot$ model in Fig. 15, with the NGC 7714 disc clusters as blue circles and bridge clusters as red asterisks. The solid black curve shows the mass of a cluster with an F814W luminosity equal to our completeness limit of $10^{5.1} \, L_\odot$, as a function of age. At lower ages, we are reaching less massive clusters, and are more deficient at older ages. For clusters less than 10 Myr old, we are complete to about $10^{4.3} \, M_\odot$, while for 10^9 years we are complete only to $10^{5.5} \, M_\odot$. The dashed black line indicates the average completeness limit of $10^{4.8} \, M_\odot$. The significance of evolutionary fading is apparent, as all of the clusters with ages $\sim 10^8$ years have masses $\geq 10^{4.5} \, M_\odot$.

Table 7. Clusters by age bin for $Z = 0.2\,Z_{\odot}$.

Age	All	Luminosity cut	Mass cut	CCF$_{30}$[a]	CCF$_{100}$[b]
1–10 Myr	59	23	13	10	10
11–22 Myr	70	28	28	12	12
23–100 Myr	2	0	1	8	78
>100 Myr	27	2	21	0	0
Total	158	53	63	30	100

[a]Expected numbers for constant cluster formation over the last 30 Myr at a rate of 1 cluster Myr^{-1}.
[b]As above for 100 Myr.

Mass cuts alter the age distributions considerably. In the $0.4\,Z_{\odot}$ model, seven of the 27 clusters remaining after eliminating those with mass $<10^{5.0}\,M_{\odot}$ are older than 22 Myr, with the youngest of these 111-Myr old. These account for six of the seven clusters remaining in the bridge (only one of which has F380W coverage) and one of six in the northern tail, but none of the 14 clusters in the southern tail.

Of the 63 clusters remaining after eliminating those with mass $<10^{4.8}\,M_{\odot}$ in the $0.2\,Z_{\odot}$ model, 31 are in the southern tail, 18 in the northern tail and 14 in the bridge. There are 22 clusters with ages >22 Myr, 12 of them in the bridge, of which five lacked coverage in F380W. In the southern tail, seven of 31 clusters are older than 22 Myr (five of them detected at 3σ level), while the northern tail has two of 18 clusters older than 22 Myr. The youngest of these clusters has an age of 89 Myr.

The number of clusters falling into each age bin in the $0.2\,Z_{\odot}$ model is summarized in Table 7 for all measured clusters, clusters above the luminosity limit and clusters above the average mass completeness limit. For comparison, we have included columns showing the expected numbers of clusters assuming a cluster formation rate of 1 cluster Myr^{-1}, and constant cluster formation for the last $10^{7.5}$ (CCF$_{30}$) and 10^8 (CCF$_{100}$) years, only including clusters above the mass limits. These are limiting cases, based on Fig. 14. The observed number of clusters in the mass limit case fall between these two limits. Thus, with the available data we cannot rule out constant cluster formation with no infant mortality. More sensitive data are needed to reduce the completeness limits and search for evidence of cluster destruction. With the current data set, the number of clusters is relatively small and the mass cut-off relatively high, thus the results on infant mortality are uncertain.

6.3 H II region age estimates

Ages for the H II regions were estimated in two ways. The colours obtained from large-aperture photometry in the *GALEX* and *HST* bands were fit to SB99 models, using the methods described in Section 5.2. In regions E and G–J, the FUV and NUV measurements provided only upper limits, so these bands were not fit to the models. The range of cluster ages within the H II regions suggests that the star formation histories are more complex than the instantaneous starbursts used to model the individual clusters. We therefore used both instantaneous and continuous star formation models to estimate the ages of these regions. The true star formation history is likely to fall between these two extremes.

Ages were also estimated using the Hα equivalent widths, which were fit to instantaneous burst SB99 models. These data are shown in Table 5, along with the median age of the *HST* clusters detected in each region. Note that the *HST* sample has no clusters in region E (four were detected but were covered in only two filters), only two

clusters in region C, since it is at the edge of the WFPC2 field of view, and in the bridge (regions G–J) only one or two clusters were found in each region, so this indicator is only useful in regions A, B, D and F. When possible, we also compare with published ages determined via photoionization modelling.

The ages determined using EW(Hα) are generally consistent with the median age of clusters found in the region, with both showing cluster population ages $\lesssim 15$ Myr. These estimates are somewhat higher than those in the literature (see Table 5), but are within a factor of ~ 3 in most of the large aperture photometry cases.

The ages determined by fitting SB99 models to the large aperture photometry of the H II regions are much higher than those determined by other methods in regions B, D and F. The area within the apertures occupied by clusters is relatively small, so it is possible that faint sources outside the clusters are making significant contributions to the total luminosity of the H II regions. If these sources are older and redder, the age of the region as a whole could be quite different from that of its bright clusters. These sources could be older clusters below our detection threshold or the remnants of clusters that have already dissolved and entered the field population.

To quantify the possible influence of faint sources on the *HST* apertures, the fraction of luminosity in the F814W band for each of the H II regions f_c originating in the measured clusters was determined. The f_c values are similar throughout the NGC 7714 disc, with ~ 80 per cent of the light coming from outside the clusters. Unresolved objects could significantly impact the colours, which may explain the higher age estimates for regions B, D and F.

All of the bridge H II regions had their lowest age estimates provided by colour fitting, while f_c varies. Regions G and I had the lowest f_c values in the system, while H and J have the highest. Visual inspection of regions G and I indicates several likely clusters that were not selected by DAOFIND. Considering the relatively high noise and low resolution in *HST* bridge data, it is likely that these results are products of the data quality. Deeper imaging will be required to learn if the bridge hosts a cluster population that differs from that of the NGC 7714 disc.

Extinction estimates are shown in Table 6, along with some values from the literature. The extinction estimates of González Delgado et al. (1995) come from the Balmer decrement, while the extinction in the nucleus found by González Delgado et al. (1999) was determined using evolutionary synthesis results for UV continuum flux distributions, and was smaller than that found using the Balmer decrement by a factor of ~ 3. Our extinction estimate for the nucleus is in good agreement with that of González Delgado et al. (1999), while our other estimates are higher than the literature values by a factor of ~ 2. This is not surprising, since the Balmer decrement tends to give higher extinction estimates than the continuum by a factor of ~ 2 (Fenelli, O'Connell & Thuan 1988; Storchi-Bergmann, Calzetti & Kinney 1994), possibly because dust in star-forming regions with strong nebular emission is destroyed or removed by ionizing radiation, stellar winds or SN (Fenelli et al. 1988). Another possibility is that the hot stars responsible for the Balmer lines are still associated with the dusty molecular clouds in which they formed, while the cooler stars that contribute to the continuum have drifted away from these regions and suffer less extinction (Calzetti et al. 1994).

6.4 *Spitzer* colours

Figs 16 and 17 show as red circles the *Spitzer* [4.5]–[5.8] versus [3.6]–[4.5] and [5.8]–[8.0] versus [4.5]–[5.8] colours of the H II regions. These were calculated from the flux densities as described
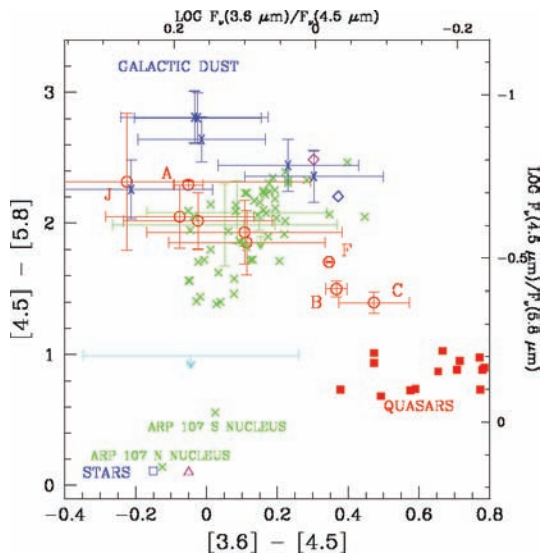
Figure 16. *Spitzer* [4.5]–[5.8] versus [3.6]–[4.5] colour–colour plot. The Arp 284 H II regions (open red circles) are shown along with emission 'clumps' from Arp 24 (Cao & We 2007), 82 (Hancock et al. 2007), 107 (Smith et al. 2005b), 285 (Smith et al. 2008) and NGC 2207/IC 2163 (Elmegreen et al. 2006; green crosses). Shown separately are Arp 285 NGC 2856 tail clump 3 (magenta open diamond) and disc clump 1 (cyan limit), as well as NGC 2207/IC 2163 'clump i' shown separately (open blue diamond). Also shown are the mean colours of field stars of Whitney et al. (2004) (magenta open triangle), M0III stars (Cohen, private communication; open blue square), quasars (Hatziminaoglou et al. 2005; red squares) and diffuse dust in the Milky Way (Flagey et al. 2006; blue crosses).
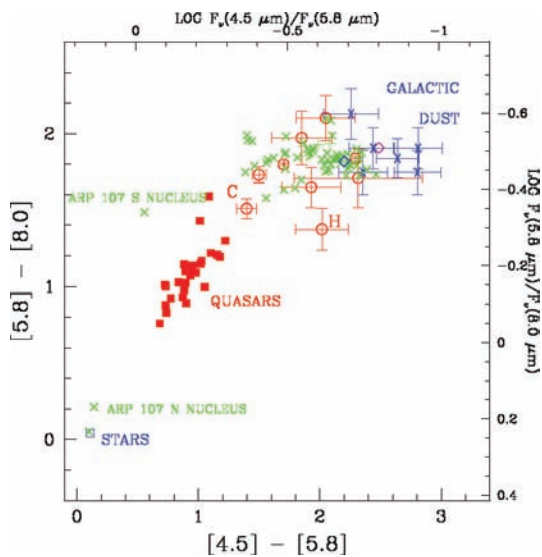
Figure 17. Same as Fig. 16, but for [5.8]–[8.0] versus [4.5]–[5.8].

in the IRAC data handbook. For comparison, we also show emission 'clumps' from several other interacting systems, including Arp 24 (Cao & We 2007), 82 (Hancock et al. 2007), 107 (Smith et al. 2005b), 285 (Smith et al. 2008) and NGC 2207/IC 2163 (Elmegreen et al. 2006), as green crosses. In the Arp 285 system, NGC 2856 tail clump 3 and disc clump 1 were unusual, and are marked in Fig. 16 as a magenta open diamond and cyan limit, respectively. The unusually luminous clump 'i' in the eastern tail of NGC 2207 is also shown separately, as an open blue diamond. We also display the mean colours of field stars of Whitney et al. (2004) (magenta

open triangle), M0III stars (Cohen, private communication; open blue square), quasars (Hatziminaoglou et al. 2005; red squares) and diffuse galactic dust (Flagey et al. 2006; blue crosses).

Most of the H II region *Spitzer* colours fit well with the clumps measured in other systems. This is important, since the selection criteria are somewhat different. The Arp 284 regions were selected based on Hα emission, whereas clumps in the other systems were selected based on *Spitzer* emission. While the Hα emission usually had a counterpart in *Spitzer* 8.0 μm, in some cases the aperture placement would have differed slightly if the 8.0 μm emission had been used for selection.

[4.5]–[5.8] is often used as a gauge of the star formation rate, with redder colours indicating higher rates of mass-normalized star formation (e.g. Smith et al. 2005b). The H II regions lie between interstellar matter and stars, indicating that, as in other interacting systems, they probably have contributions from both. However, none of the Arp 284 regions is quite as red as the Arp 285 tail clump. Smith et al. (2008) suggest that the exceptionally red colour of this clump is due to strong emission from interstellar matter owing to the very young age of the clump, which was determined to be 4 Myr using optical colours. Region J has the same estimated age and is only slightly bluer in colour, suggesting that it may also have numerous hot young stars.

The [5.8]–[8.0] colours generally fall close to those of interstellar matter, which is not surprising since the 5.8 and 8.0 μm bands are expected to be dominated by interstellar dust.

A few of the regions are unusual. Regions B and C are unusually red in [3.6]–[4.5], but slightly blue in the other two colours. Region F is redder in [3.6]–[4.5] than clumps in other systems with similar [4.5]–[5.8] colour. Region H is slightly blue in [5.8]–[8.0].

The colours of regions B and C suggest excess emission at 4.5 μm, perhaps with a slight deficiency at 5.8 and 8.0 μm, qualitatively similar to low-metallicity dwarf galaxies. In Figs 18 and 19, we compare the *Spitzer* colours of Arp 284 H II regions to those of the dwarf and spiral galaxies of Smith & Hancock (2009). Regions B and C are not as red in [3.6]–[4.5] as some the dwarfs, but are
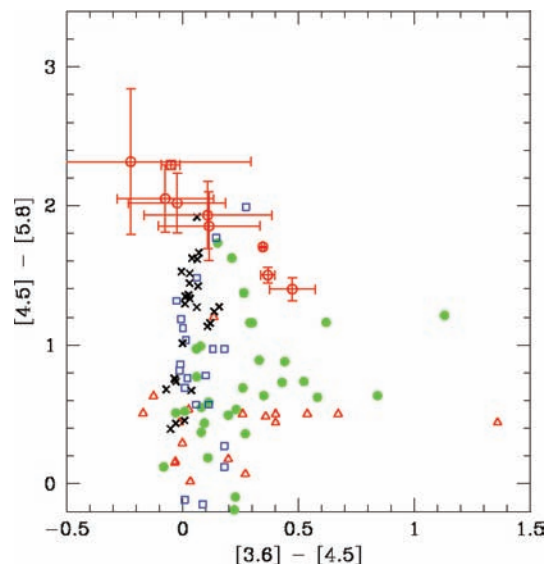

Figure 18. *Spitzer* [4.5]–[5.8] versus [3.6]–[4.5] colour–colour plot showing Arp 284 H II regions (open red circles). The dwarf galaxies of Smith & Hancock (2009) are shown by metallicity, with $12 + \log{(O/H)} < 7.9$ (red open triangles), $7.8 \leq 12 + \log{(O/H)} \leq 7.9$ (green filled circles) and $12 + \log{(O/H)} > 8.2$ (blue open squares), along with a sample of 'normal' spirals (black crosses).
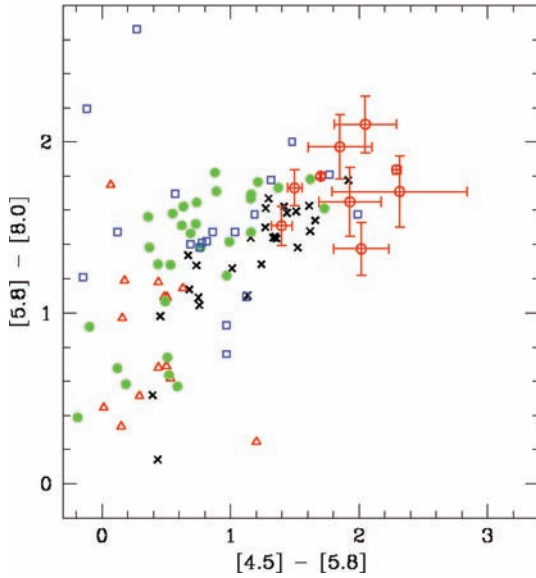
Figure 19. Same as Fig. 18, but for [5.8]–[8.0] vs. [4.5]–[5.8].
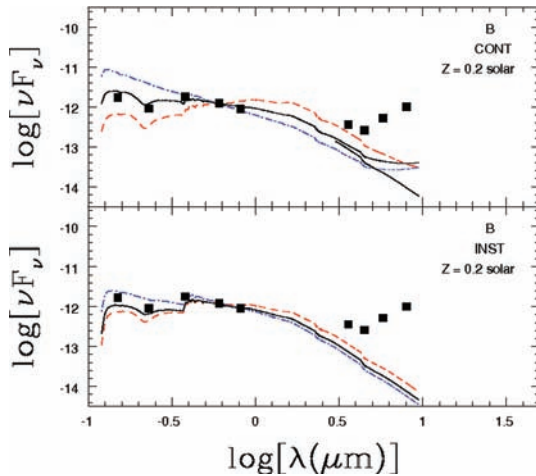

Figure 20. The FUV–mid-IR SED of region B. The black curves are the best-fitting $0.2 Z_\odot$ evolutionary synthesis models including both stellar and nebular emission. The model in the top panel is for continuous star formation with an age of 128^{+1272}_{-42} Myr, while the bottom panel shows an instantaneous burst with an age of 88^{+16}_{-18} Myr. The solid green line plotted from 3–9.5 µm shows the models without nebular emission. The short-dashed red and dot–dashed blue curves correspond to the youngest and oldest models and the associated best-fitting extinctions. The models have been scaled to match the observations in F606W.

generally redder than the spirals. This may indicate that they are deficient in PAHs, though not extremely so, consistent with their moderately low metallicities.

It is interesting that regions B and C stand out in these plots, but the other regions do not. Our colour-based age estimate for region B is very similar to that of D, and our estimates based on EW(Hα) vary little between regions. García-Vargas et al. (1997), however, found regions B and C to be extremely young. This would imply more nebular continuum and Brα emission, which are two of the factors that appear to contribute to reddening [3.6]–[4.5] in the dwarfs (Smith & Hancock 2009).

The SED for region B is plotted in Fig. 20. We also show as black curves the best-fitting $0.2 Z_\odot$ evolutionary synthesis models from
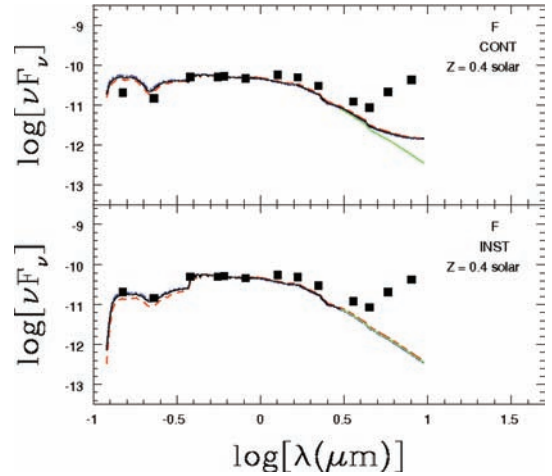

Figure 21. Same as Fig. 20, but shows region F with $0.4 Z_\odot$ models, with ages of 421^{+12}_{-11} Myr for the continuous star formation model and 222^{+6}_{-6} Myr for the instantaneous burst model.

SB99 for both continuous (top panel) and instantaneous burst (bottom panel) star formation models. The curves use the best-fitting ages for each model, which are 128^{+1272}_{-42} Myr for continuous star formation and 88^{+16}_{-18} Myr for the instantaneous star formation models. The models include both stellar and nebular emission. The solid green lines show the same models without nebular emission. The models corresponding to 1σ uncertainty (68 per cent confidence) are also shown. All of the curves have been scaled to match the observations in F606W. The stellar and stellar+nebular emission models are nearly indistinguishable, indicating that nebular emission is relatively unimportant for these inferred ages. The large mid-IR excess could result from hot dust continuum emission, PAH lines or an older stellar population, either in clusters that have faded below our detection limits or in the field. The excess is diminished in the continuous star formation model, probably because it includes older stars.

For comparison, the SED of the nucleus is shown in Fig. 21. The top panel shows curves for a continuous star formation model with an age of 421^{+12}_{-11} Myr, while the bottom panel shows an instantaneous starburst with an age of 222^{+6}_{-6} Myr. In this plot, we have also included the near-IR *J*-, *H*- and *K*-band fluxes from Lançon et al. (2001). The nucleus is known to have a complex star formation history, likely including stars older than ~100 Myr. The mid-IR excess is greater in the instantaneous burst model, likely due older stars not included in this model.

6.5 Comparison with *Chandra*

6.5.1 Ultraluminous X-ray sources

X-ray observations by Smith et al. (2005a) detected three non-nuclear point sources with $L_X > 10^{39}$ erg s^{-1}, the standard definition of an ultraluminous X-ray (ULX) source. Three other point sources lie just below this limit. The nature of ULXs is not presently understood. In one possible scenario, they could be intermediate mass (100–1000 $M_\odot$) black holes (IMBH; Colbert & Mushotzky 1999). Alternatively, they may be stellar mass black holes with beamed (King et al. 2001) or super-Eddington (Begelman 2002) X-ray emission. IMBHs may preferentially form in massive star clusters (e.g. Portegies Zwart et al. 2004a). It takes at least 4 Myr for a stellar mass black hole/X-ray binary to form, and they are

expected to be common in populations with ages up to ≈100 Myr (Rappaport, Fregau & Spruit 2004). In contrast, an IMBH may form in a YMC in ≤3 Myr (Portegies Zwart et al. 2004a). Evolutionary models of the predicted X-ray emission from IMBH+stellar companion mass-transfer binaries indicate that such ULXs should generally have ages less than about 15–30 Myr (Portegies Zwart, Dewi & Maccarone 2004a).

As discussed in Smith et al. (2005a), the ULX candidates in NGC 7714/5 exist in a range of environments. A luminous X-ray point source is located 1.5-arcsec away from the nucleus, near cluster n01, which has an estimated age of 14 Myr. If this association is correct, the young age is more consistent with the IMBH scenario. Another possibly young ULX candidate is found within H II region C, which has an age of 11 Myr based on EW(Hα) and a spectroscopically determined age of 4.5 Myr (García-Vargas et al. 1997). However, this second ULX cannot be associated with a specific star cluster, since there are several clusters very close together in the area. Finally, one ULX is located in the outer western tail of NGC 7714, in an area that is undetected in Hα but is bright in *GALEX* images. Three other ULX candidates are neither located in H II regions nor are they close to optically selected star clusters. Given the variety of environments, from this small sample we cannot make any strong conclusions about the nature of ULXs as a class.

6.5.2 Extended X-ray emission associated with star-forming regions

In addition to point sources, the *Chandra* map revealed extended X-ray emission associated with some of the H II regions (Smith et al. 2005a). Fig. 2 shows *Chandra* 0.3–8 keV X-ray contours over a colour scale Hα image of NGC 7714. Extended X-ray emission is found associated with all of the disc H II regions except D. The bridge regions G–J also do not have observed diffuse X-ray emission.

The possible contributors to the extended X-ray emission include multiple unresolved high-mass X-ray binaries (HMXBs) or hot gas from SNe and stellar winds impacting the ambient interstellar medium. Based on Local Group studies, the HMXB component is expected to be too small to account for this emission in the NGC 7714/5 regions (Smith et al. 2005a), unless there is an excess above Local Group galaxies. For the hot gas component, using SB99 models and a constant X-ray production efficiency L_X/L_{mech}, where L_{mech} is the mechanical luminosity from the SNe and winds, the ratio of the number of Lyman continuum photons N_{LyC} to X-ray luminosity N_{LyC}/L_X is expected to drop off with age for a star-forming region (Smith et al. 2005a). However, the one H II region complex in the NGC 7714 disc that is not detected in extended X-ray emission, region D, has an EW(Hα)-based age that is somewhat older than some of the other regions (Table 7), in spite of having the highest N_{LyC}/L_X. In contrast, region E is bright in the X-rays, with a low N_{LyC}/L_X, but has a younger age from its EW(Hα). This suggests that the X-ray production efficiency may vary with time and/or from region to region, and/or the HMXB contribution may be larger than expected in some regions. This result is uncertain, however, due to the relatively large uncertainties on our age estimates and the small number of H II regions in our sample.

7 CONCLUSIONS

We have used broad-band colours to obtain age estimates for 174 protoglobular cluster candidates in the Arp 284 system. The populations detected in the tidal features of NGC 7714 are generally

quite young (≲20 Myr old). However, when the sample is limited by a mass cut, the dominance of young clusters becomes unclear in the NGC 7714 disc and vanishes in the bridge. Due to the small number of clusters above the mass cut, this latter result is highly uncertain. Deeper imaging is required to better define the cluster mass function and push down the completeness limit, particularly in the bridge, which has higher photometric uncertainties and less F380W coverage than the rest of the system.

No substantial differences are found between the populations within NGC 7714. The clusters in the nucleus do not generally differ in age from those in the tidal structures. It therefore appears that the early-stage dissolution processes, if present, operate via internal processes, rather than local environmental effects, but we cannot rule out the possibility of weaker dissolution in the bridge.

Using larger apertures to study H II region complexes, we find in several cases that the region as a whole appears to be older than the clusters detected inside it. This suggests an older, redder population that is unresolved, possibly the remnants of star clusters that have already dissolved or which were not detected as discrete sources because of evolutionary fading.

The large aperture results suggest that star formation has been ongoing in H II regions B and D, located in the northern tail, for a dynamical time-scale, like that in the nucleus. In both the cases, the star formation history, whether continuous or in discrete bursts, is unknown. We also do not know if regions B and D are gravitationally bound, or simply regions where successive waves or infall events have triggered star formation. Region C is similar, but we have insufficient data to comment on its nature. If in the future these regions are found to be bound, they could be interpreted as nearby analogues to the high-redshift disc clumps studied by Elmegreen et al. (2009).

The Arp 284 interaction has been in progress for over 100 Myr, yet we find little evidence for a significant cluster population older than 20 Myr. Thus, it is possible that clusters are dissolving on a relatively short time-scale. However, due to completeness issues, with the available data we cannot definitively confirm the possibility of infant mortality in this system. Further, more sensitive observations are needed to search for a deficiency of older clusters.

REFERENCES

Arp H., 1966. Atlas of Peculiar Galaxies. Caltech, Pasadena
Bastian N., Goodwin S. P., 2006, MNRAS, 369, L9
Bastian N., Gieles M., Lamers H. J. G. L. M., Scheepmaker R. A., de Grijs R., 2005a, A&A, 431, 905
Bastian N., Hempel M., Kissler-Patig M., Homeier N. L., Trancho G., 2005b, A&A, 435, 65
Bastian N., Trancho G., Konstantopoulos I. S., Miller B. W., ApJ, 2009, 701, 607
Begelman M., 2002, ApJ, 568, L97
Bernlöhr K., 1993, A&A, 258, 25
Brandl B. R. et al., 2004, ApJS, 154, 188

Calzetti D., Kinney A. L., Storchi-Bergmann T., 1994, ApJ, 429, 582
Cao C., Wu H., 2007, AJ, 133, 1710
Colbert E., Mushotzky R., 1999, ApJ, 519, 89
Conti P. S., Vacca W. D., 1994, ApJ, 423, L97
de Gijs R., Parmentier G., 2007, Chinese J. Astron. Astrophys., 2, 155
Elmegreen D. M., Elmegreen B. G., Kaufman M., Sheth K., Struck C., Thomasson M., Brinks E., 2006, ApJ, 642, 158
Elmegreen B. G., Elmegreen D. M., Fernandez M. X., Lemoias J. J., 2009, ApJ, 692, 12
Fall S. M., Chandar R., Whitmore B. C., 2005, ApJ, 631, L133
Fanelli M. N., O'Connell R. W., Thuan T. X., 1988, ApJ, 334, 665
Fazio G. G., Hora J. L., Allen L. E., 2004, ApJS, 154, 10
Flagey N., Boulanger F., Vrestraete L., Miville Deschênes M. A., Noriega Crespo A., Reach W. T., 2006, A&A, 453, 969
García-Vargas M. L., González Delgado R. M., Pérez E., Alloin D., Díaz A., Terlevich E., 1997, ApJ, 478, 112
Gieles M., 2009, MNRAS, 394, 2126
Gieles M., Portegies Zwart S. F., Baumgardt H., Athanassoula E., Lamers H. J. G. L. M., Sipior M., Leenaarts J., 2006, MNRAS, 371, 793
González Delgado R. M., Pérez E., Díaz Á. I., García-Vargas M. L., Terlevich E., Vilchez J. M., 1995, ApJ, 439, 604
González Delgado R. M., García-Vargas M. L., Goldader J., Leitherer C., Pasquali A., 1999, ApJ, 513, 707
Goodwin S. P., Bastian N., 2006, MNRAS, 373, 752
Hancock M., Smith B. J., Struck C., Giroux M. L., Appleton P. N., Charmandaris V., Reach W. T., 2007, AJ, 133, 676
Hancock M., Smith B. J., Giroux M. L., Struck C., 2008, MNRAS, 289, 1470
Hatziminaoglou E. et al., 2005, AJ, 129, 1198
Holtzman J. A. et al., 1992, AJ, 103, 691
Holtzman J. A. et al., 1995, PASP, 107, 156
Hunter D. A., O'Connell R. W., Gallagher J. S., III, 1994, AJ, 108, 84
Hunter D. A., Elmegreen B. G., Dupuy T. J., Mortonson M., 2003, AJ, 126, 1836
James P. A. et al., 2004, A&A, 414, 23
Kennicutt R. C., Jr., 1984, ApJ, 287, 116
King A. R., Davies M. B., Ward M. J., Fabbiano G., Elvis M., 2001, ApJ, 552, L109
Kroupa P., 2002, Sci, 295, 85
Lançon A., Goldader J. D., Leitherer C., González Delgado R. M., 2001, ApJ, 552, 150
Leitherer C. et al., 1999, ApJS, 123, 3
Martin D. C. et al., 2005, ApJ, 619, L1
O'Halloran B., Metcalfe L., Delaney M., McBreen B., Laureijs R., Leech K., Watson D., Hanlon L., 2000, MNRAS, 360, 871

Portegies Zwart S. F., Dewi J., Maccarone T., 2004a, MNRAS, 355, 413
Portegies Zwart S. F., Baumgardt H., Hut P., Makino J., McMillan S. L. W., 2004b, Nat, 428, 724
Rappaport S. A., Fregeau J. M., Spruit H., 2004, ApJ, 606, 436
Smith B. J., Hancock M., 2009, AJ, 138, 130
Smith B. J., Wallin J. F., 1992, ApJ, 393, 544
Smith B. J., Struck C., Pogge R. W., 1997, ApJ, 283, 754
Smith B. J., Struck C., Nowak M. A., 2005a, AJ, 129, 1350
Smith B. J., Struck C., Appleton P. N., Charmandaris V., Reach W., Eitter J. J., 2005b, AJ, 130, 2117
Smith B. J., Struck C., Hancock M., Appleton P. N., Charmandaris V., Reach W. T., 2007, AJ, 133, 791
Smith B. J. et al., 2008, AJ, 135, 2406
Storchi-Bergmann S., Calzetti D., Kinney A. L., 1994, ApJ, 429, 572
Struck C., Smith B. J., 2003, ApJ, 289, 157
Tremonti C. A., Calzetti D., Leitherer C., Heckman T. M., 2001, ApJ, 555, 322
Vázquez G. A., Leitherer C., 2005, ApJ, 621, 695
Weedman D. W., Feldman F. R., Balzano V. A., Ramsey L. W., Sramek R. A., Wu C.-C., 1981, ApJ, 248, 105
Weisskopf M. C., Brinkman B., Canizares C., Garmire G., Murray S., Van Speybroeck L. P., 2002, PASP, 114, 1
Werner M. W. et al., 2004, ApJS, 154, 1
Whitmore B. C., Schwiezer F., Leitherer C., Borne K., Robert C., 1993, AJ, 106, 1354
Whitmore B. C., Zhang Q., Leitherer C., Fall S. M., Schweizer F., Miller B. W., 1999, AJ, 118, 1551
Whitney B. A. et al., 2004, ApJS, 154, 315
Zhang Q., Fall S. M., 1999, ApJ, 527, L81

SUPPORTING INFORMATION

Additional Supporting Information may be found in the online version of this article:

Table 2. Cluster magnitudes and age estimates:
Table 3. Cluster $E(B - V)$ and mass estimates.

Please note: Wiley-Blackwell are not responsible for the content or functionality of any supporting materials supplied by the authors. Any queries (other than missing material) should be directed to the corresponding author for the article.

This paper has been typeset from a TEX/LATEX file prepared by the author.